ISSN 0915-633X

NATIONAL INSTITUTE FOR FUSION SCIENCE

Flow Structure of Thermal Convection in a Rotating Spherical Shell

H. Kitauchi, K. Araki and S. Kida

(Received - June 28, 1996)

NIFS-426 July 1996

RESEARCH REPORT
NIFS Series

NAGOYA, JAPAN

Flow Structure of Thermal Convection in a Rotating Spherical Shell

Hideaki Kitauchi[†], Keisuke Araki[‡] and Shigeo Kida[‡]

[†] Research Institute for Mathematical Sciences. Kyoto University, Sakyo-ku, Kitashirakawa Oiwake-cho, Kyoto, 606-01. Japan

[‡] Theory and Simulation Center, National Institute for Fusion Science, Chikusa-ku, Furo-cho, Nagoya 464-01, Japan

Abstract A convoluted pattern of streamlines in a steady state of thermal convection of a Boussinesq fluid between two concentric spheres rotating with a common angular velocity is investigated numerically at Rayleigh number 3200, Taylor number 8000, Prandtl number 1, and the radius ratio 0.5 of the two spheres. Five pairs of Taylor-Proudman vortex columns with opposite rotation are generated, which arrange alternatively parallel to the axis of rotation across the middle in the equatorial plane of the spherical shell. These vortex columns retrograde at a constant angular velocity. The flow field is steady in a frame rotating with this angular velocity. The velocity filed is symmetric with respect to the equatorial plane. Two kinds of nontrivial closed streamlines which turns once around the rotating axis of the spheres and seven different kinds of non-trivial stagnation points of velocity are found in the steady flow frame. The entangled topological structure of the velocity field is resolved by visualization of closed streamlines and streamlines emanating from stagnation points.

Keywords Thermal convection, rotating spherical shell, Taylor-Proudman vortex columns, closed streamlines.

1. Introduction

The thermal convection between two concentric rotating spheres as well as in a single rotating sphere has long been studied by many researchers as one of the simplest models which represent the dynamics of melted material in the core of celestial bodies, such as the sun and the earth. The structure of it is expected to play a key role for understanding of the physics of such problems as pattern formation of core and its secular variation, magnetic field generation, etc. [1-3]. Owing to interactions between two different spatial symmetries involved, that is, the spherical symmetry of the boundaries and the axisymmetry of rotation of the shell, the flow field can be intrinsically three-dimensional and complicated entangled streamlines can be generated. In course of study of a thermally driven MHD dymano in a rotating spherical shell we have reached a conclusion that there may exist a close relation between the flow structure of the thermal convection and the mechanism of magnetic field generation [4]. This has motivated us to study the detailed structure of thermal convection as described in this paper.

The structure of thermal convection in a rotating spherical shell or a sphere has been investigated so far mostly by linear theories. Among others, Roberts [5] and Busse [6] showed by a linear stability analysis that Taylor-Proudman vortex columns develop as the most unstable mode which are arranged in parallel with the rotation axis in the middle of the equatorial plane. Later, the structure and the dynamics of these vortex columns, especially asymmetric shape of their cross-section was investigated in detail numerically as well as theoretically [7-10]. To the authors' knowledge, although there are quite a few direct numerical simulations of the full dynamical system [11, 12], the detailed flow structure of the thermal convection, which may play a dynamically important role, has not been well understood.

In this paper we describe the three-dimensional flow structure of a thermal convection. The fundamental equations of the current thermal problem and the numerical method to be employed are briefly explained in §2. The numerical results are presented in §3. After discussing the way of approach to a final steady state in §3.1, we describe the structure of the flow filed in detail; the structure of high-vorticity regions, especially the Taylor-Proudman columns in §3.2, two kinds of closed streamlines in §3.3, the locations of

stagnation points in §3.4 and the local structure of streamlines near each stagnation point as well as the global flow structure in the whole spherical shell in §3.5. Finally, section 4 is devoted for concluding remarks.

2. Formulations

We consider the motion of a Boussinesq fluid of density ρ in two concentric spheres of radii r_1 and r_2 $(= r_1 + d)$ rotating with a common constant angular velocity $\boldsymbol{\Omega}$ (see figure 1). The temperature is kept uniform both on the inner and the outer spheres and constant at all the time. It is hotter on the inner sphere than on the outer by ΔT, which drives a thermal convection. There is gravity force $\boldsymbol{g} = -\rho\gamma\boldsymbol{r}$ which is pointed to the center, where γ is a constant and $\boldsymbol{r}$ is a position vector relative to the center of the spheres. Then, a set of equations describing the time-evolution of the flow field are written, in a frame rotating with the spheres, as

$$\frac{\partial \boldsymbol{u}}{\partial t} = -\nabla P + \alpha\gamma T\boldsymbol{r} + \boldsymbol{u} \times (\nabla \times \boldsymbol{u}) + 2\boldsymbol{u} \times \boldsymbol{\Omega} + \nu\nabla^2\boldsymbol{u}, \tag{2.1}$$

$$\frac{\partial T}{\partial t} = -\nabla \cdot (\boldsymbol{u}T) + \kappa\nabla^2 T, \tag{2.2}$$

$$\nabla \cdot \boldsymbol{u} = 0, \tag{2.3}$$

where $\boldsymbol{u}$ is the velocity, $P = p/\rho + \frac{1}{2}|\boldsymbol{u}|^2 + \frac{1}{2}\gamma|\boldsymbol{r}|^2 - \frac{1}{2}|\boldsymbol{\Omega} \times \boldsymbol{r}|^2$ is a modified pressure, α is the thermal expansion coefficient, T is the temperature, ν is the kinematic viscosity of fluid, and κ is the thermal diffusivity. The boundary conditions for the velocity and the temperature are given by

$$\boldsymbol{u} = \boldsymbol{o}, \quad T = \Delta T \quad \text{at} \quad r = r_1, \tag{2.4}$$

$$\boldsymbol{u} = \boldsymbol{o}, \quad T = 0 \quad \text{at} \quad r = r_2. \tag{2.5}$$

In order to non-dimensionalize these equations we measure length by thickness d of the spherical shell, time by thermal diffusion time d^2/κ, and temperature by temperature difference ΔT between the two spheres, and introduce non-dimensional variables (denoted by asterisk) as

$$\boldsymbol{r} = \boldsymbol{r}^* d, \quad t = t^* \frac{d^2}{\kappa}, \quad \boldsymbol{u} = \boldsymbol{u}^* \frac{\kappa}{d}, \quad T = T^* \Delta T, \quad P = P^* \frac{\kappa^2}{d^2}. \tag{2.6}$$

By substituting (2.6) into (2.1)−(2.3), we obtain, after omitting the asterisks,

$$\frac{\partial \boldsymbol{u}}{\partial t} = -\nabla P + P_r R_a T \boldsymbol{r} + \boldsymbol{u} \times (\nabla \times \boldsymbol{u}) + P_r T_a^{\frac{1}{2}} \boldsymbol{u} \times \hat{\boldsymbol{z}} + P_r \nabla^2 \boldsymbol{u}, \tag{2.7}$$

$$\frac{\partial T}{\partial t} = -\nabla \cdot (\boldsymbol{u} T) + \nabla^2 T, \tag{2.8}$$

$$\nabla \cdot \boldsymbol{u} = 0, \tag{2.9}$$

where

$$P_r = \frac{\nu}{\kappa} \tag{2.10}$$

is the Prandtl number,

$$R_a = \frac{\alpha \gamma \Delta T d^4}{\kappa \nu} \tag{2.11}$$

is the Rayleigh number,

$$T_a = \left(\frac{2|\boldsymbol{\Omega}| d^2}{\nu} \right)^2 \tag{2.12}$$

is the Taylor number, and $\hat{\boldsymbol{z}} = \boldsymbol{\Omega}/|\boldsymbol{\Omega}|$ is the unit vector along the rotation axis. Boundary conditions (2.4) and (2.5) are respectively rewritten as

$$\boldsymbol{u} = \boldsymbol{o}, \quad T = 1 \quad \text{at} \quad r = \eta/(1-\eta), \tag{2.13}$$

$$\boldsymbol{u} = \boldsymbol{o}, \quad T = 0 \quad \text{at} \quad r = 1/(1-\eta), \tag{2.14}$$

where $\eta = r_1/r_2$ is the radius ratio of the two spheres.

Equations (2.7)−(2.9) are solved numerically by the pseudo-spectral method. The solenoidal velocity field is expressed in terms of toroidal and poloidal vector fields as

$$\boldsymbol{u}(r, \vartheta, \varphi, t) = \nabla \times \nabla \times (V(r, \vartheta, \varphi, t)\hat{\boldsymbol{r}}) + \nabla \times (W(r, \vartheta, \varphi, t)\hat{\boldsymbol{r}}) \tag{2.15}$$

(see Appendix III in [1]). Both the defining scalars of the poloidal and the toroidal fields are respectively expanded in spherical harmonics $Y_{lm}(\vartheta, \varphi)$ in the ϑ- and the φ-directions as

$$V(r, \vartheta, \varphi, t) = \sum_{l=0}^{L} \sum_{m=-l}^{l} V_{lm}(r, t)\, Y_{lm}(\vartheta, \varphi), \tag{2.16}$$

$$W(r, \vartheta, \varphi, t) = \sum_{l=0}^{L} \sum_{m=-l}^{l} W_{lm}(r, t)\, Y_{lm}(\vartheta, \varphi). \tag{2.17}$$

Each radial function in the above expression is further expanded in terms of Chebyshev polynomials $T_n(x)$ $(0 \leq n \leq N)$, where $x = (2r - r_1 - r_2)/(r_2 - r_1)$. A similar expansion is employed for temperature as well. The expanded modes in the present numerical simulation are truncated at $L = 31$ and $N = 32$. Aliasing errors which appear in the calculation of the non-linear terms are not removed. (We have checked that a dealiased calculation under the same condition as the aliased one showed no substantial difference in the flow structure.) Time-integration is performed by the use of the second-order Adams-Bashforth scheme for the non-linear terms and the second-order Crank-Nicolson scheme for the viscous term with time increment $\Delta t = 0.01$. The Chebyshev-tau method is employed in order to satisfy continuity equation (2.9) and boundary conditions (2.13) and (2.14) accurately.

Equations (2.7)−(2.9) under boundary conditions (2.13) and (2.14) permit a stationary thermal conduction state,

$$\boldsymbol{u} = \boldsymbol{o}, \quad T = \frac{\eta}{(1-\eta)^2}\frac{1-(1-\eta)r}{r}. \tag{2.18}$$

A linear stability analysis shows that this state is stable if the Rayleigh number is smaller than a critical value which varies depending on T_a, P_r and η. In the present simulation we set parameters as $R_a = 3200$, $T_a = 8000$, $P_r = 1$ and $\eta = 0.5$ for which thermal conduction state (2.18) is linearly unstable. The initial velocity and the temperature fields are generated by uniform random small perturbations superimposed on stationary state (2.18).

3. Results

3.1. Initial growth and equilibrium state

The growth in magnitude of the flow field is monitored in the development of total kinetic energy $\mathcal{E}(t) = \iiint \frac{1}{2}|\boldsymbol{u}|^2 \mathrm{d}^3\boldsymbol{x}$, the integration being carried out over the whole spherical shell, which is shown against time t in figures 2. The initial stage is enlarged in figure 2(b). It begins to increase exponentially in time, then looks to saturate once by $t \approx 0.9$. However, it increases slightly around $t = 1.6$, and thereafter stays constant. The total kinetic energy at the final computation time is about 550, thus the root-mean-square velocity is 6.1. The slight change of energy around $t = 1.6$ is closely related with a competition in

magnitude of the largest two Fourier modes as discussed below.

The orthogonal properties of the toroidal and the poloidal vector fields defined by (2.16) and (2.17) allow us to express the kinetic energy as a sum of energies of the individual modes, i.e.

$$\mathcal{E}(t) = \sum_{l=0}^{L} \sum_{m=-l}^{l} E_{lm}, \tag{3.1}$$

where E_{lm}'s are defined by

$$E_{lm} = \frac{l^2(l+1)^2}{2} \int_{r_1}^{r_2} \frac{(V_{lm}(r))^2}{r^2} dr + \frac{l(l+1)}{2} \int_{r_1}^{r_2} \left(\frac{\mathrm{d}V_{lm}(r)}{\mathrm{d}r} \right)^2 dr + \frac{l(l+1)}{2} \int_{r_1}^{r_2} (W_{lm}(r))^2 dr. \tag{3.2}$$

The longitudinal pattern of the convection is characterized by the azimuthal modal energy

$$\mathcal{E}_m(t) = \begin{cases} \sum_{l=0}^{L} E_{l0} & (m = 0), \\ \sum_{l=0}^{L} (E_{lm} + E_{l\,-m}) & (m > 0). \end{cases} \tag{3.3}$$

We plot in figures 3 the time-development of modal energies of the first 12 azimuthal wavenumbers as well as some of higher harmonics of wavenumber 5. The initial stage is enlarged in figure 3(b) for the largest three modes. In the initial stage all the modal energies grow exponentially in time. Mode 6 is largest in amplitude until $t \approx 1.6$ when mode 5 overtakes it.

All of these modal energies saturate by $t \approx 0.9$, and remain almost constant for a while. Around $t = 1.6$, however, they exhibit a rapid change in amplitude, and the largest amplitude mode is exchanged from $m = 6$ to 5. This corresponds to a slight change in the kinetic energy around $t = 1.6$. This exchange of the largest amplitude mode also manifests itself as the change in the number of vortex columns (see figures 6 below).

After this exchange the behavior in time-development of modal energies is classified into three groups. The first one is those modes of azimuthal wavenumbers of multiples of 5, which eventually approach to some nonzero finite values. The second is those of

wavenumbers of multiples of 5 ± 1. which decay exponentially in time with decay rate of about -0.027. The third is those of wavenumbers of multiples of 5 ± 2. which decay more rapidly with decay rate of about -0.055. Therefore the flow approaches to a five-fold rotationally symmetric state as time progresses. In passing, the above decay rates of the decaying modes should represent those for small disturbances to the final steady state.

The sudden change of the Fourier amplitudes may be understood as follows. There may be at least two equilibrium states, one of which is unstable and the other is stable. At first. the flow field happens to approach to an unstable equilibrium state along a stable manifold. But because it is unstable, the flow field can not reach this equilibrium state. Even if it stays around the equilibrium state for some while, it eventually escapes from it along an unstable manifold and is captured by a stable equilibrium state.

3.2 Taylor-Proudman vortex columns

According to the linear stability analysis of stationary thermal conduction state (2.18) in a rotating sphere, a number of pairs of vortex columns with opposite rotation are generated at some finite distance apart from the axis of rotation as marginally unstable modes [6]. This marginal field is symmetric with respect to the equatorial plane, i.e.

$$\begin{cases} u_r(r,\vartheta,\varphi,t) = u_r(r,\pi-\vartheta,\varphi,t), \\ u_\vartheta(r,\vartheta,\varphi,t) = -u_\vartheta(r,\pi-\vartheta,\varphi,t), \\ u_\varphi(r,\vartheta,\varphi,t) = u_\varphi(r,\pi-\vartheta,\varphi,t), \\ T(r.\vartheta,\varphi,t) = T(r,-\vartheta,\varphi,t). \end{cases} \tag{3.4}$$

As shown in figure 4(a), the flow field developed in the present non-linear system has the same symmetry as (3.4) do, where we plot iso-surfaces of vorticity magnitude $|\omega| = 52$ in region $1.15\ r_1 \leq r \leq 0.91\ r_2$ at $t = 25$. Here, high-vorticity regions near the spherical surfaces are omitted for better representation (see below). The black surfaces represent the cyclones (which rotate in the same direction as the spheres), while the gray the anti-cyclones. Ten vortex columns with different senses of rotation are generated alternatively along the axis of rotation lying around the middle in the equatorial plane of the spherical shell. Notice that the anti-cyclones are fatter than the cyclones, implying that vorticity in

the former is larger than in the latter.

In figure 4(b), we plot the contour of the z-component of vorticity $\omega_z = 0, \pm 52$ on the equatorial plane at $t = 25$. The dark and light regions denote positive and negative vorticity, respectively. Vorticity magnitude takes a local maximum at the center of each vortex column. The maximum of vorticity magnitude in the anti-cyclones is about 1.7 times larger than that in the cyclones. The core size of the anti-cyclones is also larger than in the cyclones. This difference in intensity is consistent with vortex stretching and shrinking which are taking place in the respective vortex columns (see figure 10(b) in §3.5). There exist stronger vorticity regions on the inner and the outer spheres. Actually, the vorticity takes a minimum (or maximum) value -148 (or 156) at the centers of negative (or positive) vorticity boundary layers on the inner sphere. If we drew iso-surfaces of vorticity magnitude over all the spherical shell in figure 4(a), the Taylor-Proudman vortex columns would have been hided by them. This is the reason why we omitted these strong vorticity boundary layers near the inner and the outer spheres in figure 4(a).

Iso-surfaces of vorticity magnitude $|\omega| = 52$ near the inner sphere $r_1 \leq r \leq 1.15 r_1$, and the outer sphere $0.91 r_2 \leq r \leq r_2$ at $t = 25$ are drawn in figures 5(a) and (b), respectively. The black surfaces represent the positive vorticity ($\omega_z > 0$), while the gray the negative ($\omega_z < 0$). These boundary layer vorticities are generated by swirling motion induced by nearby Taylor-Proudman vortex columns. Thickness of inner and outer boundary layers, which is estimated by the maximum distance of the nearest null-point of $\omega_z = 0$ from each boundary on the equatorial plane (see figure 4(b)), is about $0.15(r_2 - r_1)$ and $0.18(r_2 - r_1)$, respectively.

These vortex columns move westward as a whole. The variation in the longitude-time plane of the z-component of vorticity on the middle circle on the equatorial plane is shown in figures 6. The black regions denote the positive vorticity (anti-cyclones) and the white the negative (cyclones). The initial stage is enlarged in figure 6(b). Six pairs of vortex columns of opposite sense of rotation are generated in the initial period and established by $t = 0.9$. However, two neighboring cyclones merge into one around $t = 1.6$, and later the resulting five pairs move steadily westward without changing their relative positions with angular velocity Ω_V of about -1.24 (which is much smaller than the angular velocity of the

spherical shell $\Omega = 44.7$). This disappearance of one pair of vortex columns around $t = 1.6$ corresponds to the exchange of the largest amplitude mode from $m = 6$ to 5 observed in figures 3.

3.3. Closed Streamlines

As seen in the preceding section the vortex columns retrograde steadily with angular velocity -1.24 so that the flow field is seen to be steady in a frame rotating with this angular velocity. Notice that the velocity on the outer and the inner spheres move eastward in this moving frame.

Since the flow field is symmetric with respect to the equatorial plane, the velocity field is two-dimensional in this plane, namely, there is no flow across it. In figure 7 drawn are streamlines on the equatorial plane. The flow direction is indicated by arrows. By comparing with the contours of ω_z (figure 4(b)). we find that all the streamlines connect the centers of the nearest neighboring cyclones and anti-cyclones. A streamline which spirals out of the center of a cyclone anti-clockwise spirals into that of the next anti-cyclones of either side clockwise.

Off the equatorial plane, on the other hand, the flow field is more complicated because of intrinsic three-dimensional character of the flow configuration. It may be a usual practice to draw streamlines for understanding of the flow structure. However, almost all streamlines are too much complicated to represent the flow structure neatly. They are entangled chaotically by themselves and/or with each other. Normally it is hard to expect the existence of any nontrivial simple streamlines in this kind of system. Nevertheless we have tried to draw many streamlines to get some idea of the flow structure. Surprisingly enough, we have found two kinds of nontrivial simple closed streamlines in either of each hemisphere. These closed streamlines were found while the velocity vector field is traced numerically starting from some arbitrary positions.† These closed streamlines

† Streamlines were traced by integrating the velocity vector field numerically with a 4-th order Runge-Kutta method. The starting points were chosen arbitrary. Most of the streamlines turn eastward around the rotation axis. After many turns (typically a few hundreds times), almost all streamlines are attracted to a closed streamline at lower

in the northern hemisphere are shown in figures 8 which are viewed from three different angles. The flow direction is indicated by arrows. They close themselves after a single turn eastwardly around the rotation axis of the spherical shell. They are five-fold symmetric around the rotation axis. As is recognized in (a) and (b), the one which is located at lower latitude runs through the anti-cyclones: it comes into an anti-cyclone from the inner-sphere side, spirals up around the central axis of the anti-cyclone, escapes out of the top, then makes a turn to the east and goes around the outer-sphere side of the next eastern cyclone while approaching the equatorial plane and comes to the next eastern anti-cyclone, which completes a fundamental cycle of 1/5 of the period of the closed streamline. The other closed streamline which is located at higher latitude (cf. (a) and (c)) runs toward higher latitude along the inner sphere near a line which connects a cyclone and the pole, makes a turn upward at some higher latitude near the pole, then goes down along the outer sphere near the middle of the tops of the neighboring cyclone and anti-cyclone, and makes another turn to the east toward the middle of the next eastern cyclone and the pole. This completes a fundamental cycle of the periodic pattern of the five-fold symmetric closed streamline. The mean velocity along the closed streamline at higher latitude is 8.2 which is faster than the root-mean-square velocity 6.1 over the whole shell, while that along the lower-latitude closed streamline is 4.0 which is slower. These two closed streamlines will be used as references in the following discussion of the flow pattern.

3.4. Stagnation Points

Another key element which characterizes the flow structure is a stagnation point (if any) and flow pattern around it [13]. As depicted in figures 9 from three different angles, we found, in the present flow, 50 stagnation points except for 4 trivial ones which lie at

---

latitude. Also tried was a backward integration, that is, the streamlines were traced for a velocity vector field with reversed direction. Then, almost all streamlines were attracted to another closed streamline. This surprising finding of attracting closed streamlines in a solenoidal vector field may be attributed to possible systematic error inherent in the numerical scheme employed because there cannot exist any closed attractors in a solenoidal field.

the cross-points of the rotation axis with the outer and the inner spheres. There are ten stagnation points on the equatorial plane and fifteen in each hemisphere. Since the flow field is five-fold symmetric around the rotation axis, there are five equivalent stagnation points off the rotation axis. These stagnation points are classified into seven groups. A number attached to each stagnation point in figure 9(a) denotes different groups. Those stagnation points labeled with numbers 4—7 are located on the equatorial plane. The ones with numbers 4 and 5 are respectively at the center of cyclones and anti-cyclones, while those with numbers 6 and 7 are respectively in the vicinity of the inner and the outer spheres. The other three kinds of stagnation points are located somewhat close to the closed streamlines at higher latitude (cf. figures 8 and 9). In the following a stagnation point with number # will be cited as SP#.

3.5. Flow Structure

Now we scrutinize the flow structure of the current thermal convection velocity field. Since the flow field is five-fold symmetric around the rotation axis, it is sufficient to analyze only a fundamental region of it. In figures 10, we draw several typical streamlines such as two closed streamlines and streamlines connecting each stagnation point in a piece of the northern hemisphere of longitude width $\frac{5}{16}\pi$ which contains one anti-cyclone and two cyclones. The flow direction is shown with arrows.

The topological structure of velocity field in the vicinity of each stagnation point is characterized by a set of three eigen-values and associated left-eigen-vectors of velocity gradient tensor $\nabla \boldsymbol{u}$. Since this tensor of rank three is real, two cases are possible, namely, either all of the three eigen-values are real or one is real and the other two are conjugate complex. The sum of the real parts of the three eigen-values vanishes because the velocity field is solenoidal. According to the sign of the real part of an eigen-value a streamline either goes out of or comes into a stagnation point along the direction of the eigen-vector associated with the eigen-value. If an eigen-value is complex, the streamline makes a spiral curve on a plane spanned by the real and the imaginary parts of the associated complex eigen-vector.

Eigen-values and associated left-eigen-vectors of the velocity-gradient tensor numeri-

cally obtained at seven stagnation points are tabulated in Table I. An eigen-value is given at the top in each entry. Triplets of numbers at the bottom denote the direction of the associated eigen-vectors in the spherical coordinate (r, ϑ, φ). For a real eigen-value they represent bi-directional unit vectors parallel to the direction of the associated eigen-vector, while for a complex eigen-value a unit rotation vector normal to a plane spanned by the real and the imaginary parts of the associated complex eigen-vector and pointed in the direction of translation of a right-handed screw when it is turned in the direction given by the eigen-value. Comments on these eigen-values and eigen-vectors will be made below on discussion of the properties of streamlines connecting each stagnation point.

Although there are three eigen-streamlines connecting each stagnation point, we can, in general, trace numerically only two of them that have either the maximum or the minimum eigen-values. The former (an outgoing streamline) is traced by integrating the velocity field numerically starting from a point in the very vicinity of a stagnation point, while the latter (an incoming streamline) by integrating the velocity field with reversed sign. Therefore we can draw in general four streamlines from each stagnation point, two of which emanate from the point and the other two approach to it. The streamlines shown in figures 10(b-d) are obtained starting from points apart from each stagnation point by 10^{-4} radians in the longitude.

In figure 10(a) shown are parts of closed streamlines discussed in §3.3. The one at higher latitude turns around an SP2 (see also figure 8); it flows toward the rotation axis along the inner sphere, rises up to the outer sphere near the pole, and turn toward the lower latitude along the outer sphere, then makes another turn toward the east somewhere near the top of a cyclone to come close to the next SP2. The closed streamline at lower latitude, on the other hand, turns outside a cyclone, enters in the neighboring anti-cyclone from the inner-sphere side, spirals up once, then escapes out of it from the top, and makes a turn around the next neighboring cyclone while going down to the equator.

Streamlines which pass through four stagnation points (SP4 — SP7) are shown in figure 10(b). Since the velocity field is symmetric with respect to the equatorial plane, there is no flow across it. Therefore the velocity field is purely two-dimensional on this plane though it is not divergence-free. The flow spirals out of an SP4 at the center of

a cyclone anti-clockwise, while it spirals into an SP5 at the center of an anti-cyclone clockwise. The other two stagnation points, SP6 and SP7. are connected to the above two and constitute separatrices of streamlines (see figure 7 for streamlines on the equatorial plane). There are streamlines coming straight down to an SP4 and going up from an SP5 in the direction perpendicular to the equatorial plane. Notice that two equivalent streamlines are drawn off the equatorial plane which originate from two SP4's in figure 10(b). (All of these behaviors of the streamlines can be understood well by referring to the eigen-values and the eigen-vectors shown in Table I.) It is seen that they are traced back around an SP2, where they turn around it in a similar way as the closed streamline at higher latitude does (see figure 8(c)).

Streamlines which pass through SP1's are shown in figure 10(c), where again two equivalent lines are drawn starting from two equivalent SP1's. Both of the incoming streamlines arrive from the west after several turns around an SP2. The outgoing streamlines, on the other hand, run around somewhat parallel to a meridional plane. The one which runs down to the lower latitude comes to the equatorial plane along a cyclone, makes a turn near the plane toward the neighboring anti-cyclone. enters into it from the inner-sphere side, spirals up while shrinking its radius, and escapes out of it from the top, then makes another turn around the next cyclone just like as the outgoing streamline from an SP5 (see figure 10(b)).

Streamlines connecting either an SP2 or an SP3 are drawn together in figure 10(d). Around the SP2 the flow comes in roughly along a line connecting SP2 and SP3 and spirals out perpendicularly. On the contrary, around the SP3 the flow goes out along the above line and spirals in perpendicularly. Those streamlines that spiral out of the SP2 will follow a spiral-in orbit of the SP3 for a while but eventually run away eastward toward the next cyclone. The streamline spiraling in the SP3 looks to be more or less similar to the closed streamline at lower attitude (cf. figure 10(a)). It is remarkable that many streamlines tend to rotate roughly along meridional planes around three stagnation points SP1, SP2 and SP3. The positiveness of the longitudinal component of the rotation vectors for them shown in Table I indicates actually this direction of swirling motions.

By synthesizing all the typical streamlines shown in figures 10, we may understand

(at least a part of) the convoluted three-dimensional structure of the velocity field. In figure 11(a) drawn are some of the streamlines piked up from figures 10. Figure 11(b) is an illustration cartoon to give a simple idea on the flow structure which may be summarized as follows.

On the equatorial plane the flow spirals in the anti-cyclones clockwise, and spirals out of the cyclones anti-clockwise. The flow spirals up in an anti-cyclone, while it spirals down in a cyclone. Streamlines are skewed like a left-handed screw in the both vortex columns (which is opposite in the southern hemisphere). There are two characteristic global streams roughly along the two closed streamlines discussed in §3.3. At relatively low latitude the flow runs eastward as a whole, while meandering between the two kinds of vortex columns. Characteristic at higher latitude is the swirling flows around stagnation points SP1—SP3 between the shoulders of the cyclones and the pole in addition to the eastward global motion.

4. Concluding remarks

The flow structure of a thermal convection in a rotating spherical shell was analyzed in detail. A three-dimensional convoluted structure of the velocity field was clarified by visualization with several typical streamlines such as global closed streamlines and streamlines connecting with stagnation points.

In our contemporary simulation study of a thermally driven MHD dynamo in a rotating spherical shell the topological structure of the streamlines as well as the characteristics of the rate-of-strain and the velocity-gradient tensors have been found to have a close relation with the spatial structure of strong magnetic field [4]. The present analysis is therefore expected to be useful for understanding of the mechanism of magnetic field generation. This work will be published elsewhere soon.

Acknowledgments

We would like to express our cordial gratitude to Drs. A. Kageyama and T. Watanabe and other members of our complexity simulation group in National Institute for Fusion Science for their invaluable comments and discussions as well as their kind help in visu-

alization procedures. This work was partially supported by a Grant-in-Aid for Scientific Research from the Ministry of Education, Science and Culture.

References

[1] Chandrasekhar, S. 1968 *Hydrodynamic and Hydromagnetic Stability.* New York: Dover.

[2] Busse, F.H. 1978 Magnetohydrodynamics of the Earth's Dynamo. *Ann. Rev. Fluid Mech.* **10**, 435-62.

[3] Roberts, P.H. 1988 Future of Geodynamo Theory, *Geophys. Astrophys. Fluid Dyn.* **44**, 3-31.

[4] Araki K and Kida S (in preparation).

[5] Roberts, P.H. 1968 On the Thermal Instability of a Rotating-Fluid Sphere Containing Heat Sources, *Philos. Trans. R. Soc. London Ser. A* **263**, 93-117.

[6] Busse, F. H. 1970 Thermal Instabilities in Rapidly Rotating Systems. *J. Fluid Mech.* **44**, 441-60.

[7] Zhang K 1992 Spiraling Columnar Convection in Rapidly Rotating Spherical Fluid Shells, *J. Fluid Mech.*, **236**, 535-56.

[8] Yano J 1992 Asymptotic Theory of Thermal Convection in Rapidly Rotating Systems, *J. Fluid Mech.*, **243**, 103-31.

[9] Kida S 1994 Stability of Thermal Convection in a Rapidly Rotating Sphere *J. Pays. Soc. Japan* **63**, 2964-73.

[10] Takehiro S and Hayashi Y Y 1995 Boussinesq Convection in Rotating Spherical Shells — a Study on the Equatorial Superrotation, *The Earth's Central Part: Its Structure and Dynamics, ed. Yukutake T, Terra Sci. Pub. Co.*, pp. 123-56.

[11] Kageyama A, Watanabe K and Sato T 1993 Simulation Study of a Magnetohydrodynamic Dynamo: Convection in a Rotating Spherical Shell, *Phys. Fluids B* **5**, 2793-805.

[12] Glatzmaier G A and Roberts P H 1995 A Three-Dimensional Self-Consistent Computer Simulation of a Geomagnetic Field Reversal, *Nature* **377**, 203-9.

[13] Chong M S and Perry A E 1990 A General Classification of Three-Dimensional Flow Fields, *Phys. Fluids A*, **2**, 765-77.

Figure Caption

Figure 1. Configuration of the system

Figure 2. Time-development of total kinetic energy $\mathcal{E}(t)$. The initial stage of (a) is enlarged in (b).

Figure 3. Time-development of azimuthal modal energies $\mathcal{E}_m(t)$. A number attached to each curve denotes azimuthal wavenumber m. The initial stage of (a) is enlarged in (b) for the three largest modal energies.

Figures 4. (a) Iso-surface of vorticity magnitude $|\omega| = 52$ in region $1.15r_1 \leq r \leq 0.91r_2$ at $t = 25$. The black and gray surfaces represent the cyclones and the anti-cyclones, respectively. (b) Contour of the z-component of vorticity $\omega_z = 0, \pm 52$ on the equatorial plane. The dark regions denote the positive vorticity, while the light regions the negative.

Figure 5. Iso-surface of vorticity magnitude $|\omega| = 52$ near (a) the inner sphere $r_1 \leq r \leq 1.15r_1$ and (b) the outer sphere $0.91r_2 \leq r \leq r_2$ at $t = 25$. The black surfaces represent the positive vorticity ($\omega_z > 0$), while the gray the negative ($\omega_z < 0$).

Figure 6. Time-variation of the z-component of vorticity on the middle circle in the equatorial plane. It is positive in the black regions and negative in the white. The initial stage of (a) is enlarged in (b).

Figure 7. Streamlines on the equatorial plane at $t = 25$. Arrows denote the flow direction.

Figures 8. (a) Two closed streamlines viewed from the north pole, (b) the lower-latitude streamlines and (c) the higher-latitude streamlines. Arrows denote the flow direction. $t = 25$.

Figures 9. Stagnation points viewed from (a) the north pole, (b) the equatorial plane and (c) an oblique angle. A number attached to each point indicates seven different kinds of points with five equivalence each. $t = 25$.

Figures 10. (a) Two closed streamlines, and streamlines which pass through (b) SP4—SP7, (c) SP1 and (d) SP2 and SP3. Arrows denote the flow direction. $t = 25$.

Figure 11. Topology of velocity field. (a) Two closed streamlines and streamlines passing through SP1, SP3, SP4, SP6 and SP7 are drawn. (b) Cartoon illustrating the structure of convoluted streamlines.

SP1	5.32 $(\pm 0.27, \pm 0.80, \mp 0.54)$	$-2.66 + 3.64$ i $(-0.44, -0.37, 0.82)$	$-2.66 - 3.64$ i $(-0.44, -0.37, 0.82)$
SP2	$1.19 + 2.21$ i $(0.56, 0.61, 0.56)$	$1.19 - 2.21$ i $(0.56, 0.61, 0.56)$	-2.38 $(\pm 0.59, \mp 0.08, \pm 0.81)$
SP3	3.18 $(\pm 0.07, \pm 0.59, \pm 0.80)$	$-1.59 + 2.27$ i $(-0.35, 0.73, 0.58)$	$-1.59 - 2.27$ i $(-0.35, 0.73, 0.58)$
SP4	$1.63 + 8.33$ i $(0.00, -1.00, 0.00)$	$1.63 - 8.33$ i $(0.00, -1.00, 0.00)$	-3.26 $(0.00, \pm 1.00, 0.00)$
SP5	2.26 $(0.00, \pm 1.00, 0.00)$	$-1.13 + 14.00$ i $(0.00, 1.00, 0.00)$	$-1.13 - 14.00$ i $(0.00, 1.00, 0.00)$
SP6	1.05 $(\mp 0.03, 0.00, \pm 1.00)$	0.11 $(0.00, \pm 1.00, 0.00)$	-1.16 $(\pm 0.03, 0.00, \pm 1.00)$
SP7	0.98 $(\pm 0.05, 0.00, \pm 1.00)$	0.52 $(0.00, \pm 1.00, 0.00)$	-1.50 $(\mp 0.03, 0.00, \pm 1.00)$

Table I. Eigen-values and associated left-eigen-vectors of the velocity-gradient tensor at stagnation points. There are three eigen-values, either real or complex, at each stagnation point. Figures at the top in each entry denote eigen-values. Triplets of numbers in brackets indicate the direction of the associated eigen-vectors in the spherical polar coordinate (r, ϑ, φ). For a real eigen-value they represent bi-directional unit vectors parallel to the associated eigen-vectors, whereas for a complex eigen-value a unit vector normal to a plane spanned by the real and the imaginary parts of the associated eigen-vector and pointed in the direction in which a right-handed screw translates when it is turned in the direction given by the eigen-value.

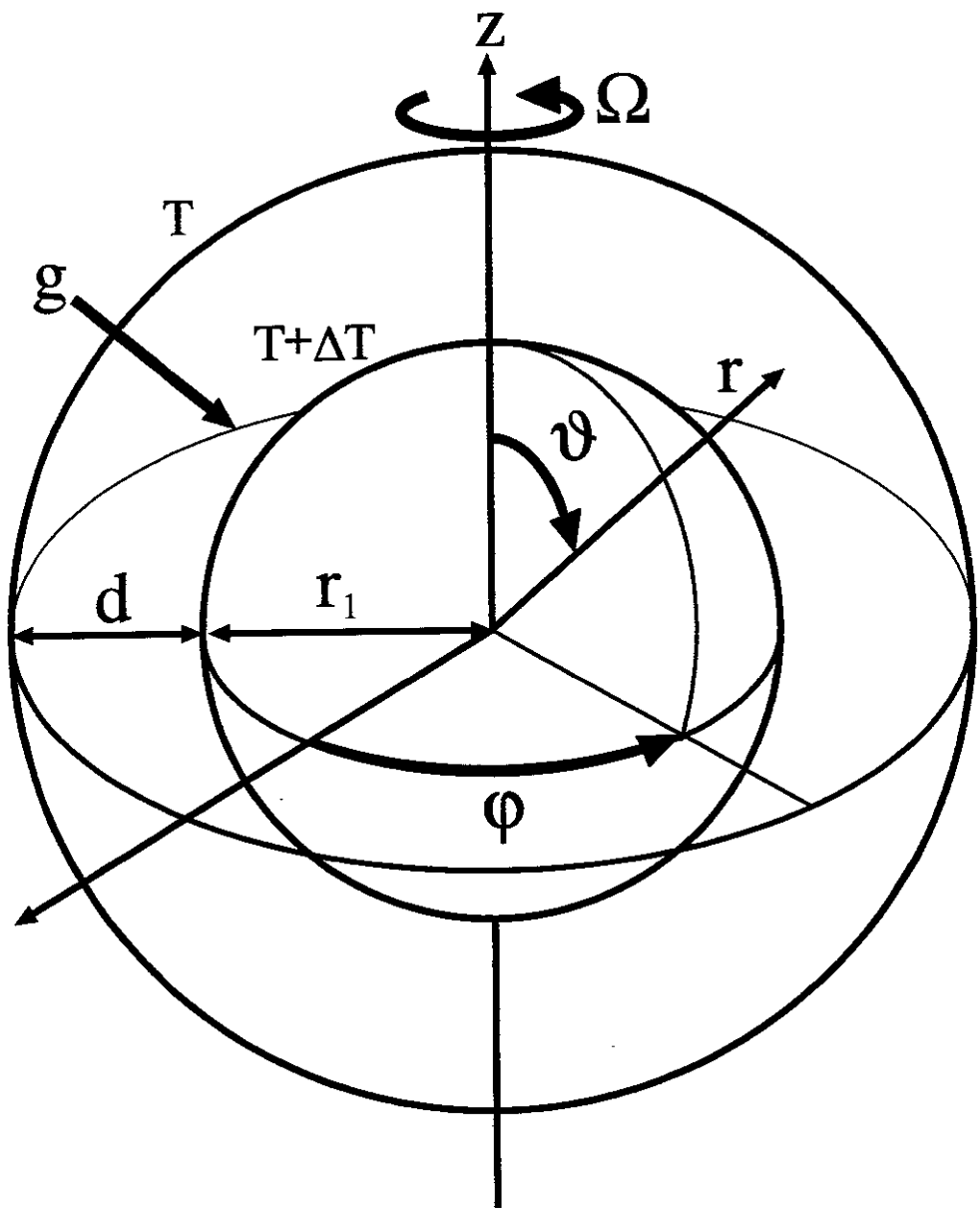

Fig.1

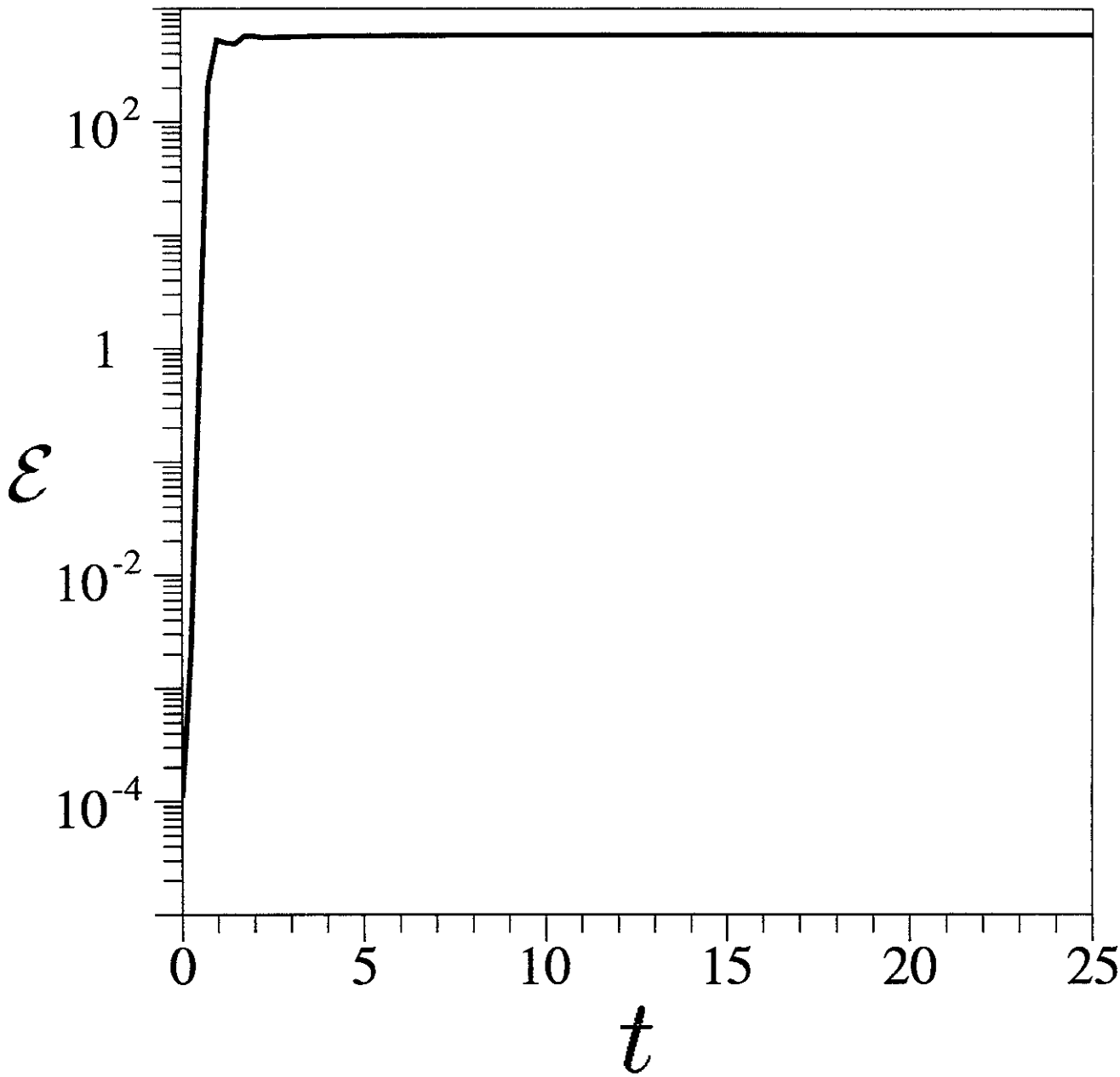

Fig.2(a)

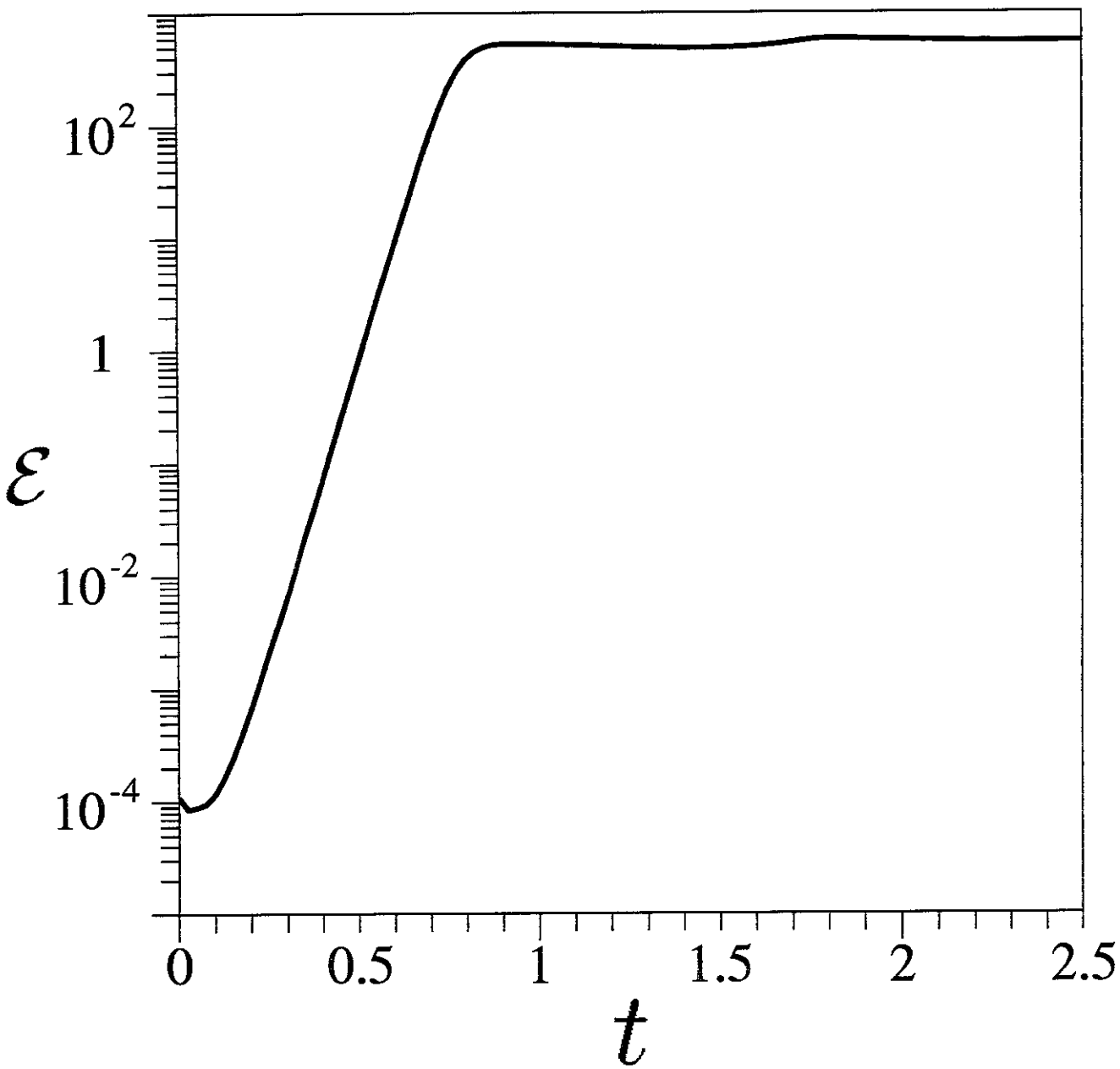

Fig.2(b)

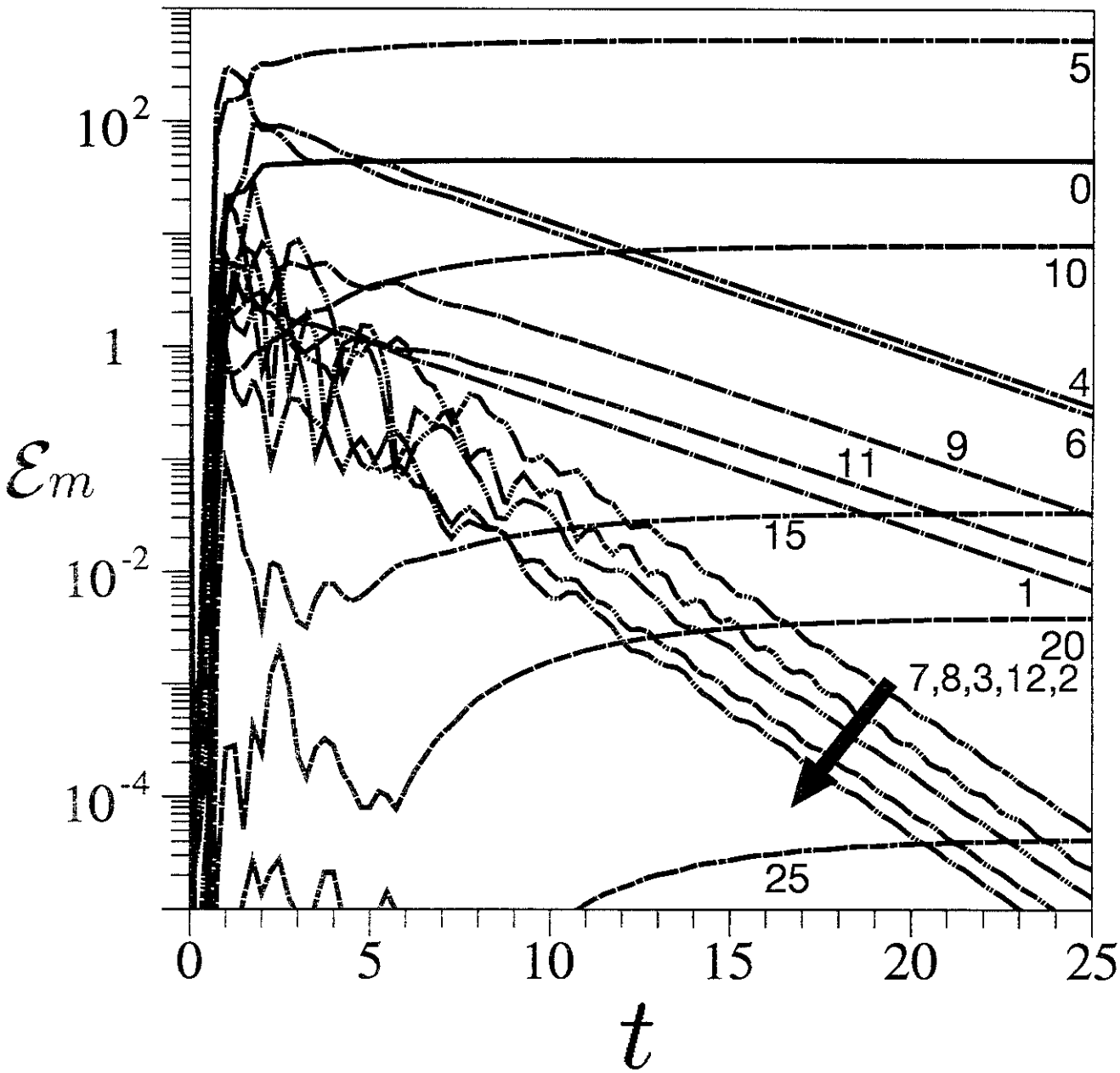
10^2
1
10^{-2}
10^{-4}
$\mathcal{E}_m$
5
0
10
4
6
9
11
15
1
20
7,8,3,12,2
25
0
5
10
15
20
25
t

Fig.3(a)

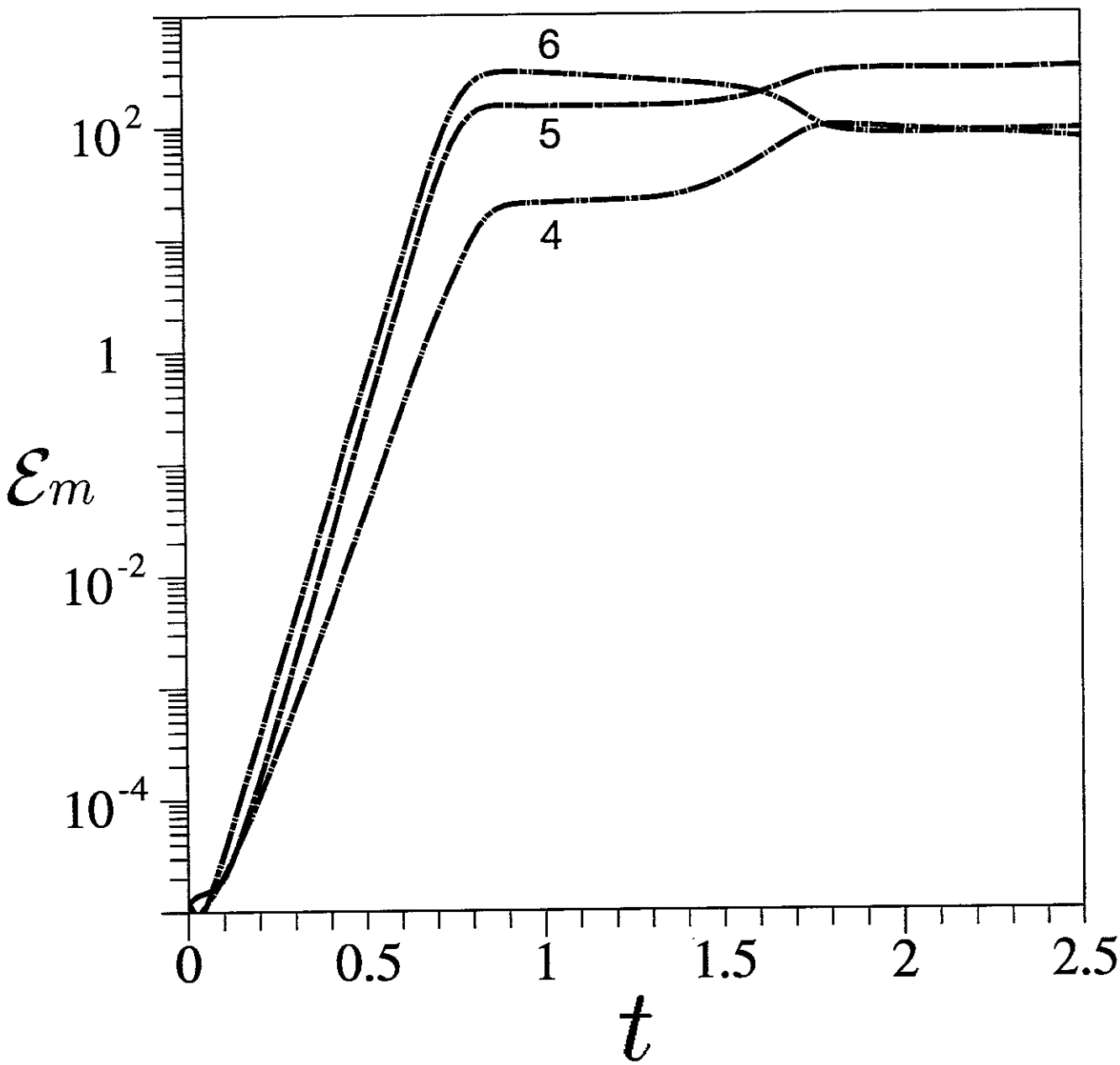

Fig.3(b)

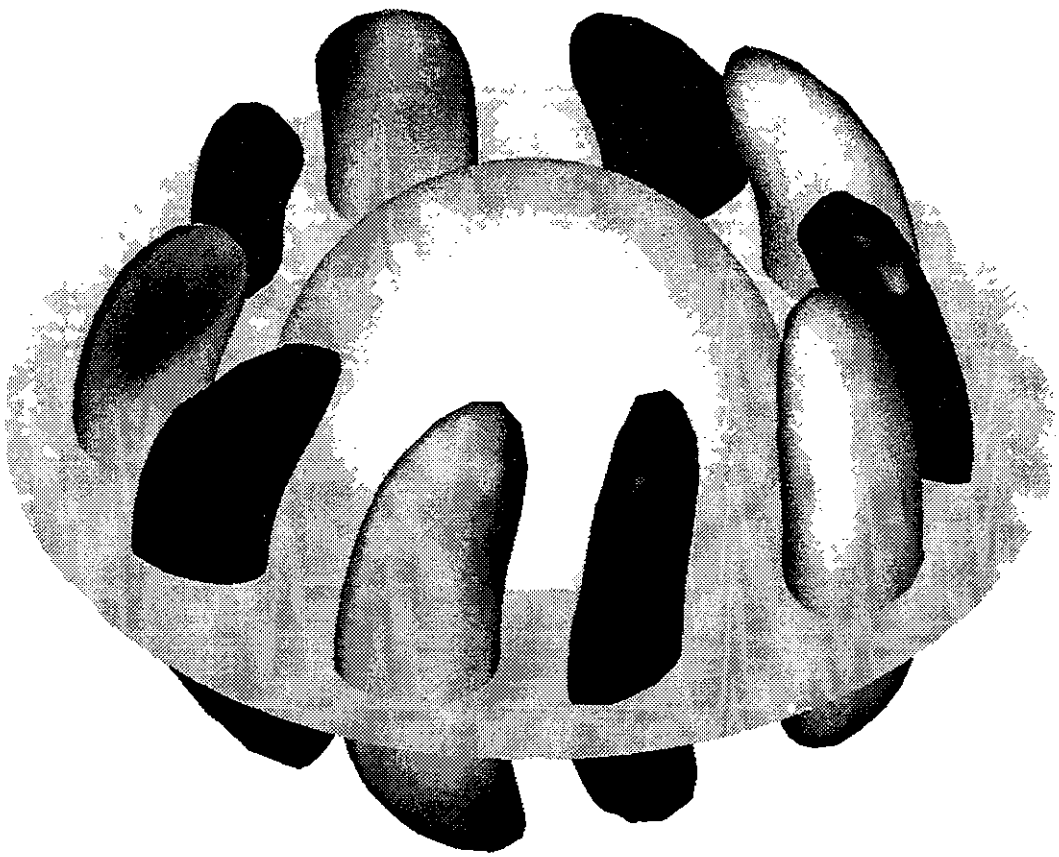

Fig.4(a)

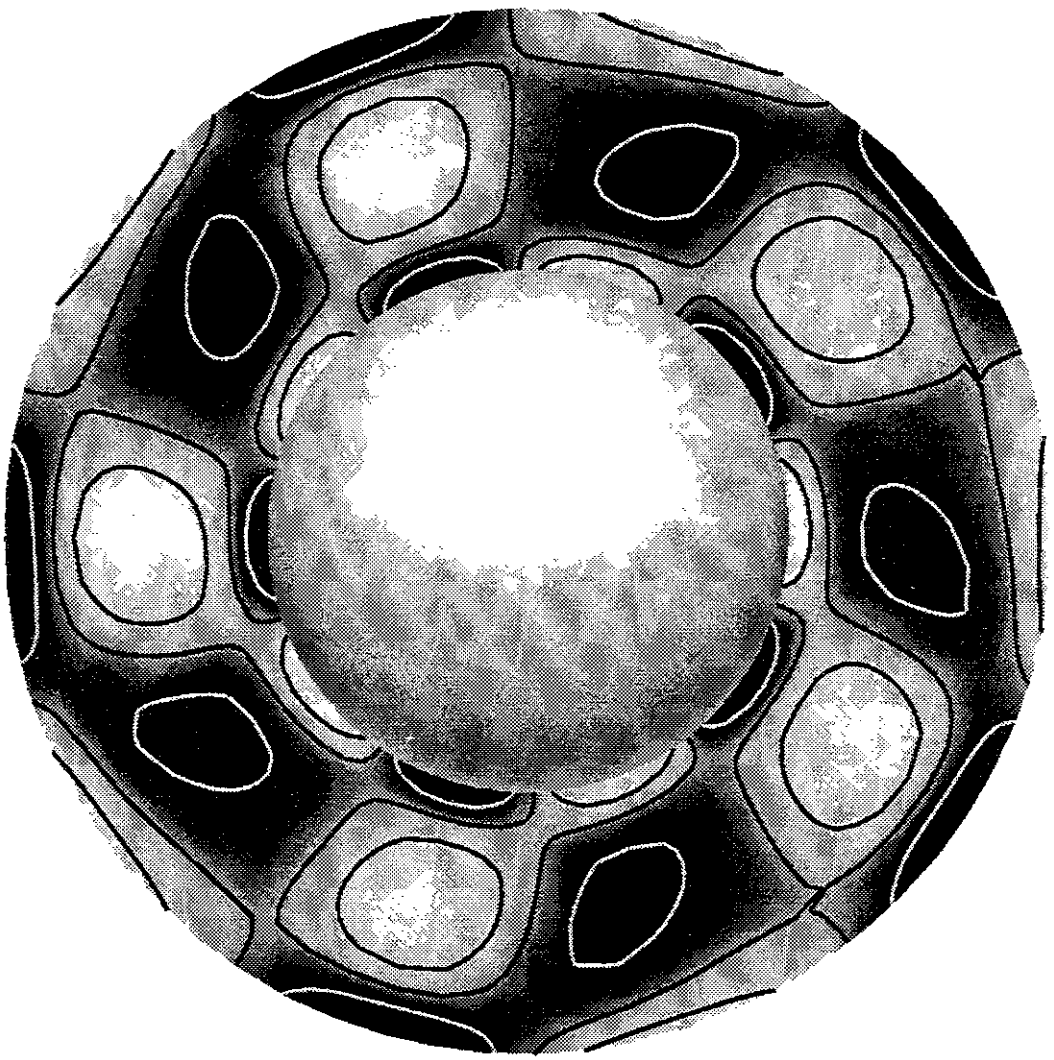

Fig.4(b)

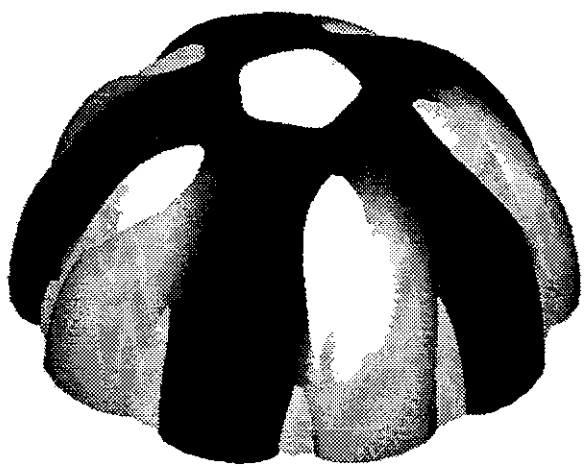

Fig.5(a)

Fig.5(b)

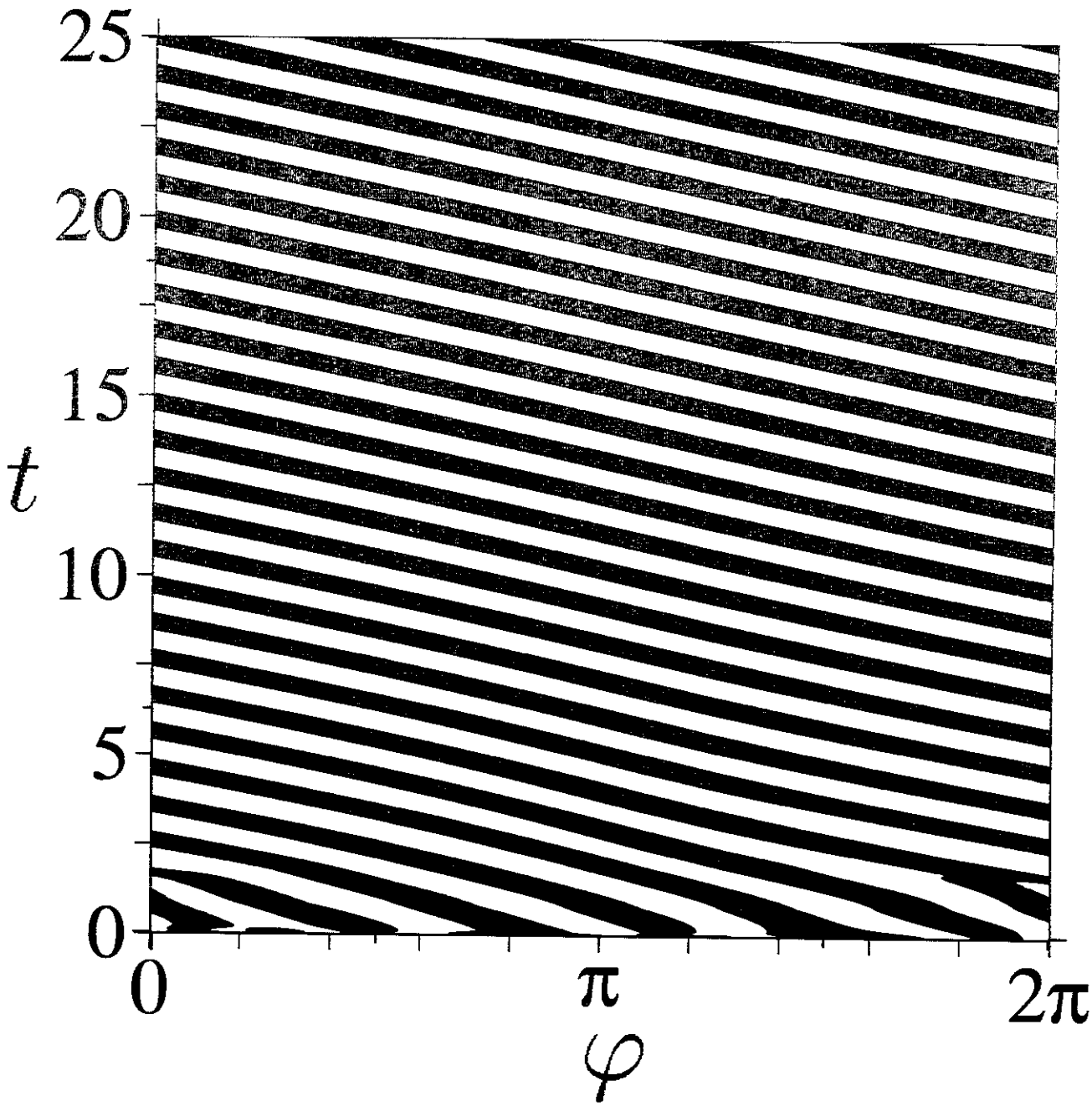

Fig.6(a)

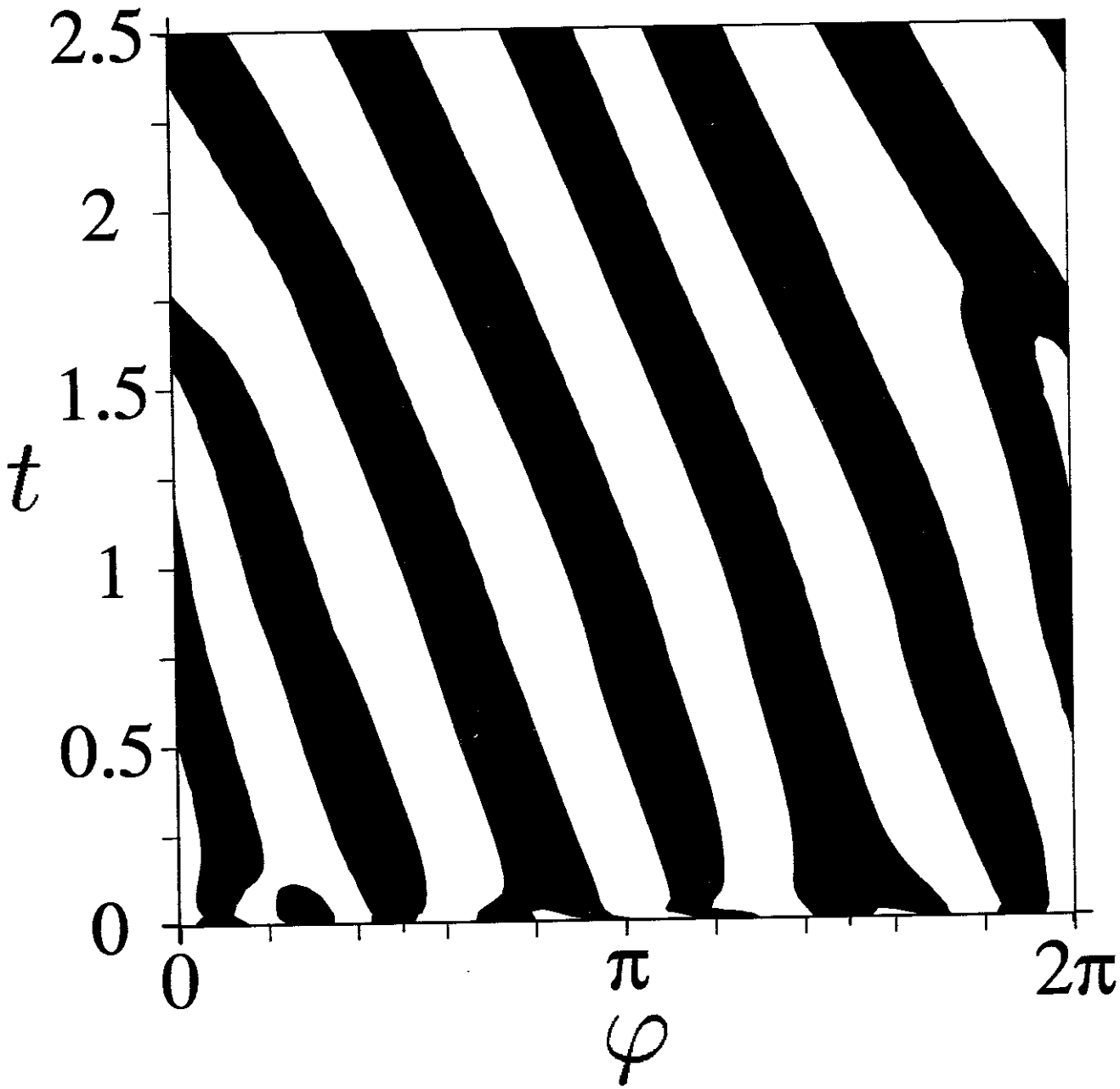

Fig.6(b)

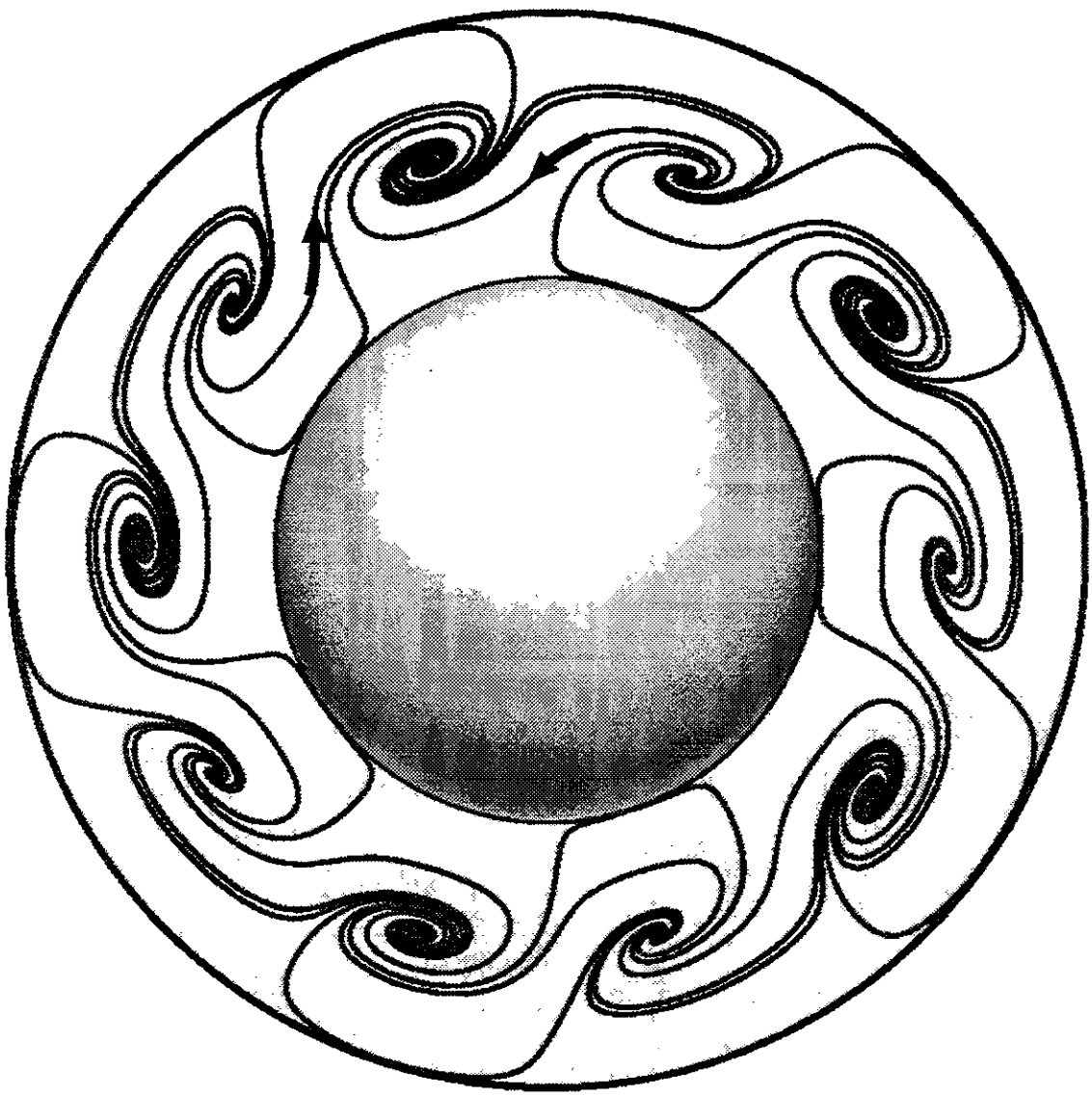

Fig.7

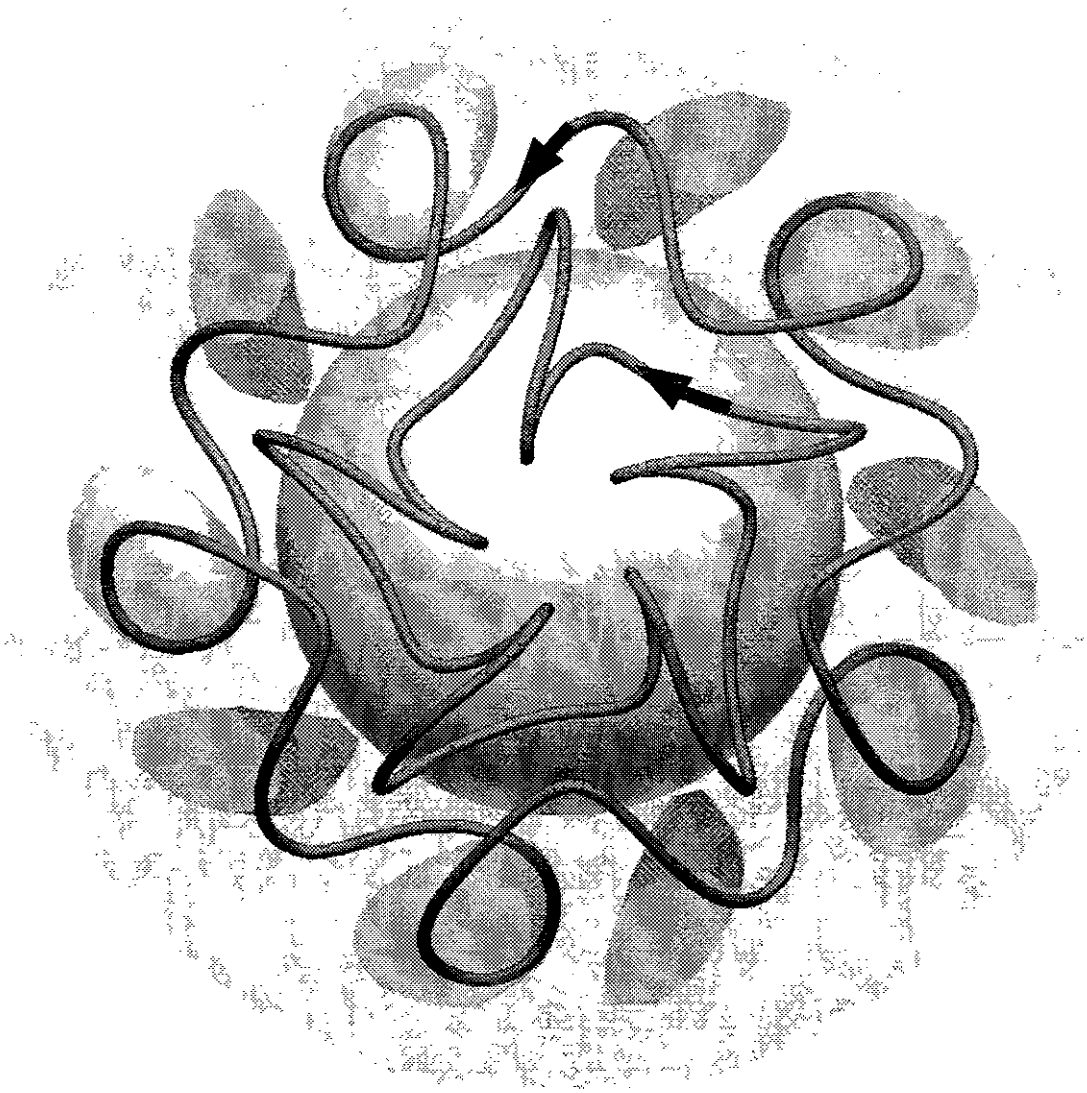

Fig.8(a)

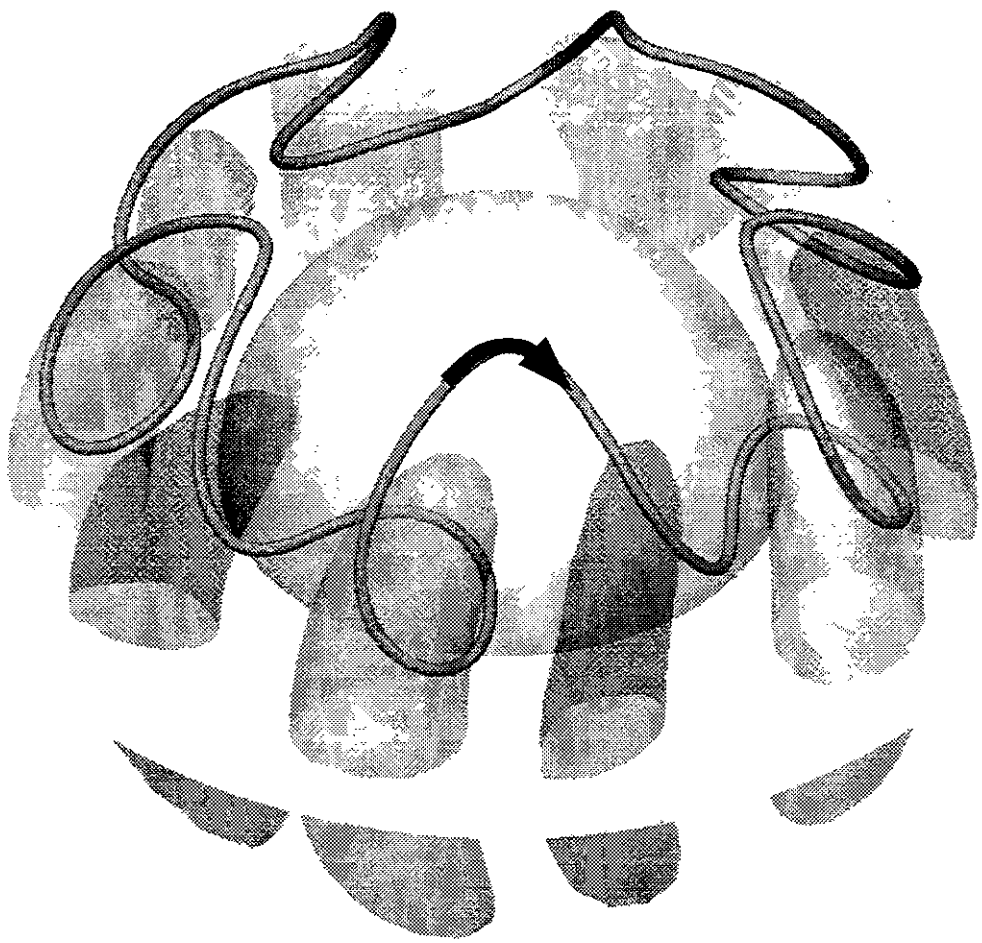

Fig.8(b)

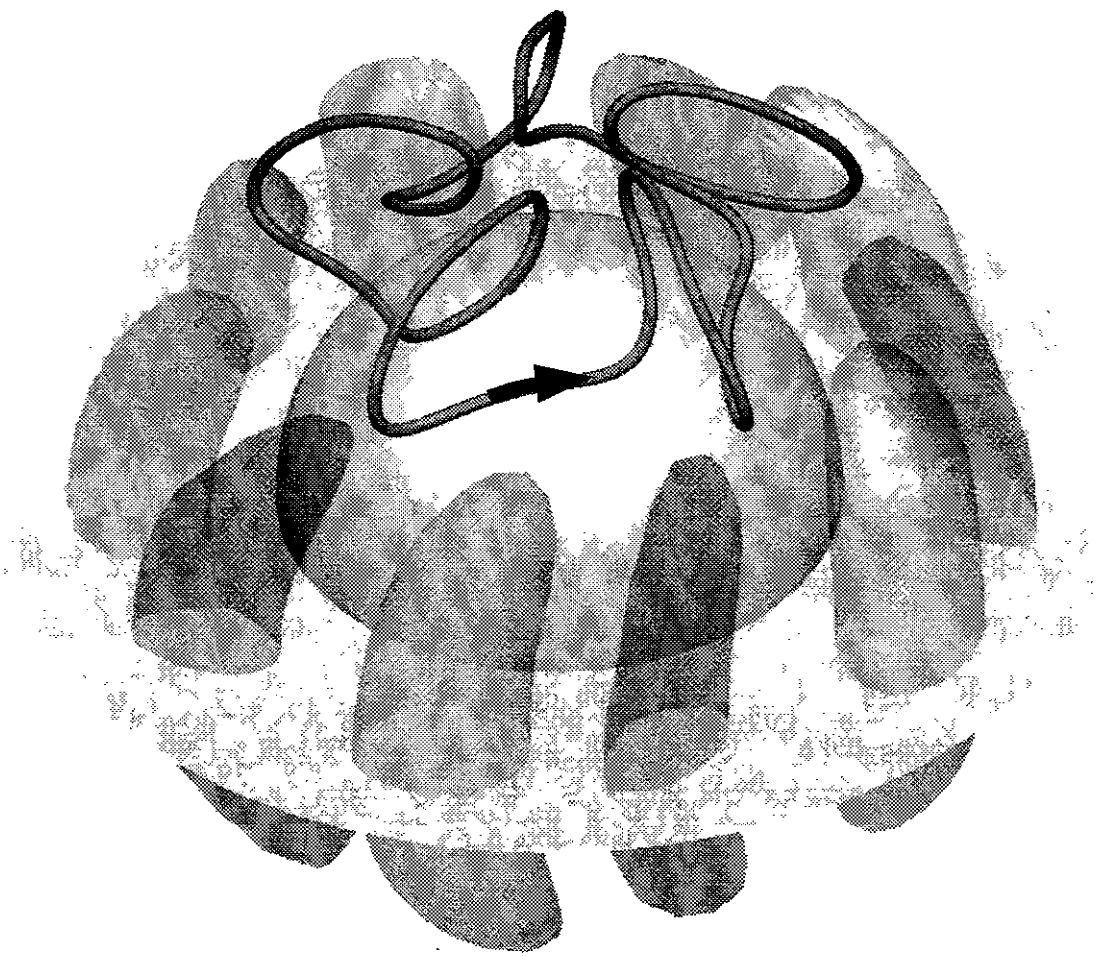

Fig.8(c)

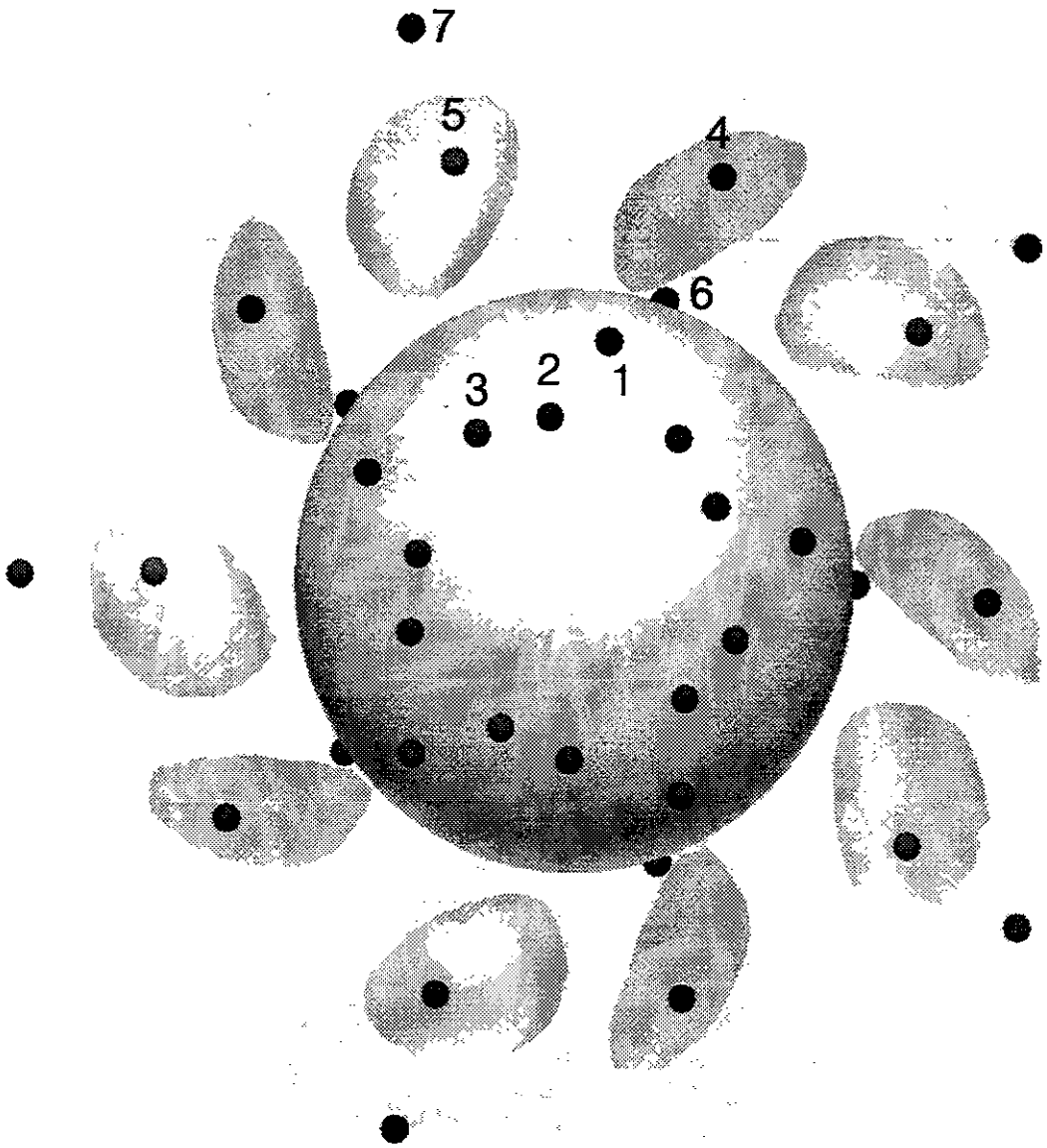

Fig.9(a)

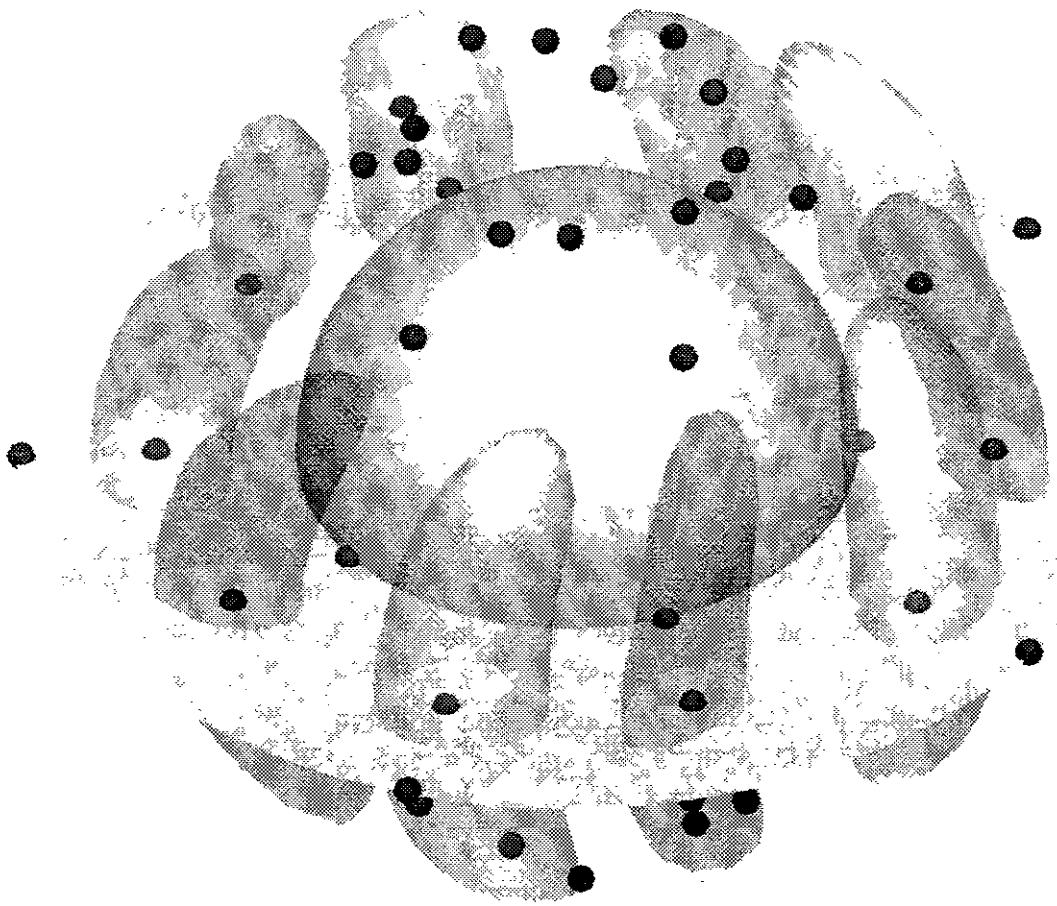

Fig.9(b)

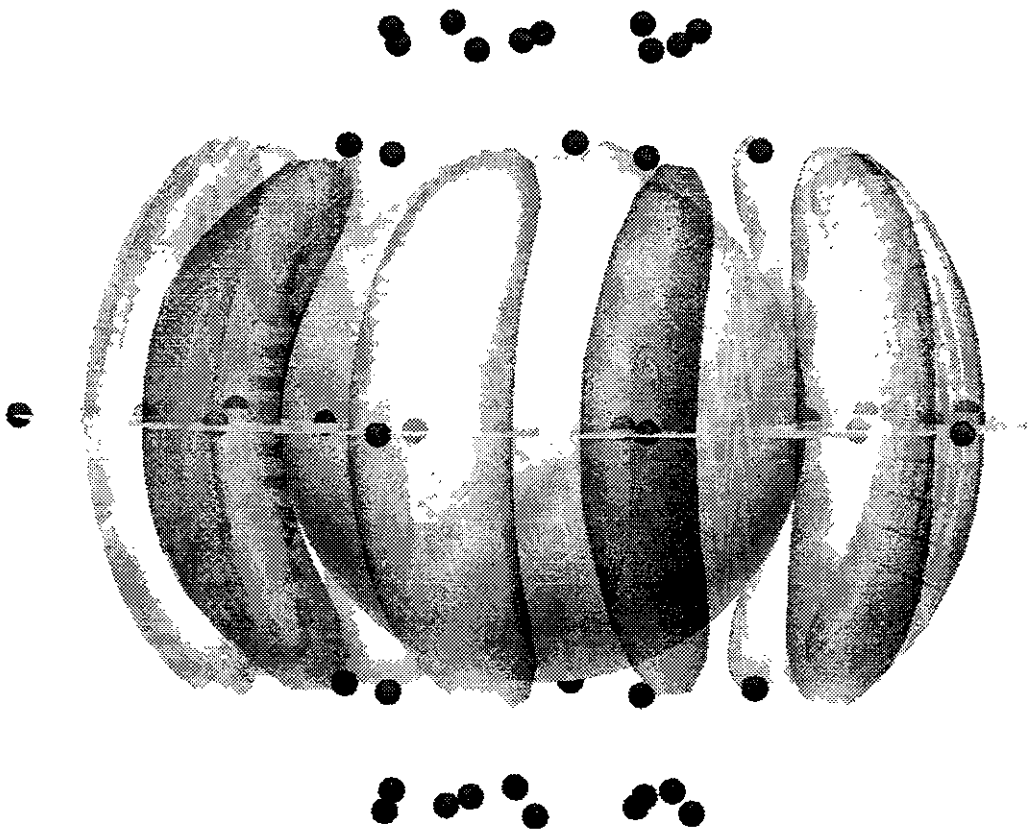

Fig.9(c)

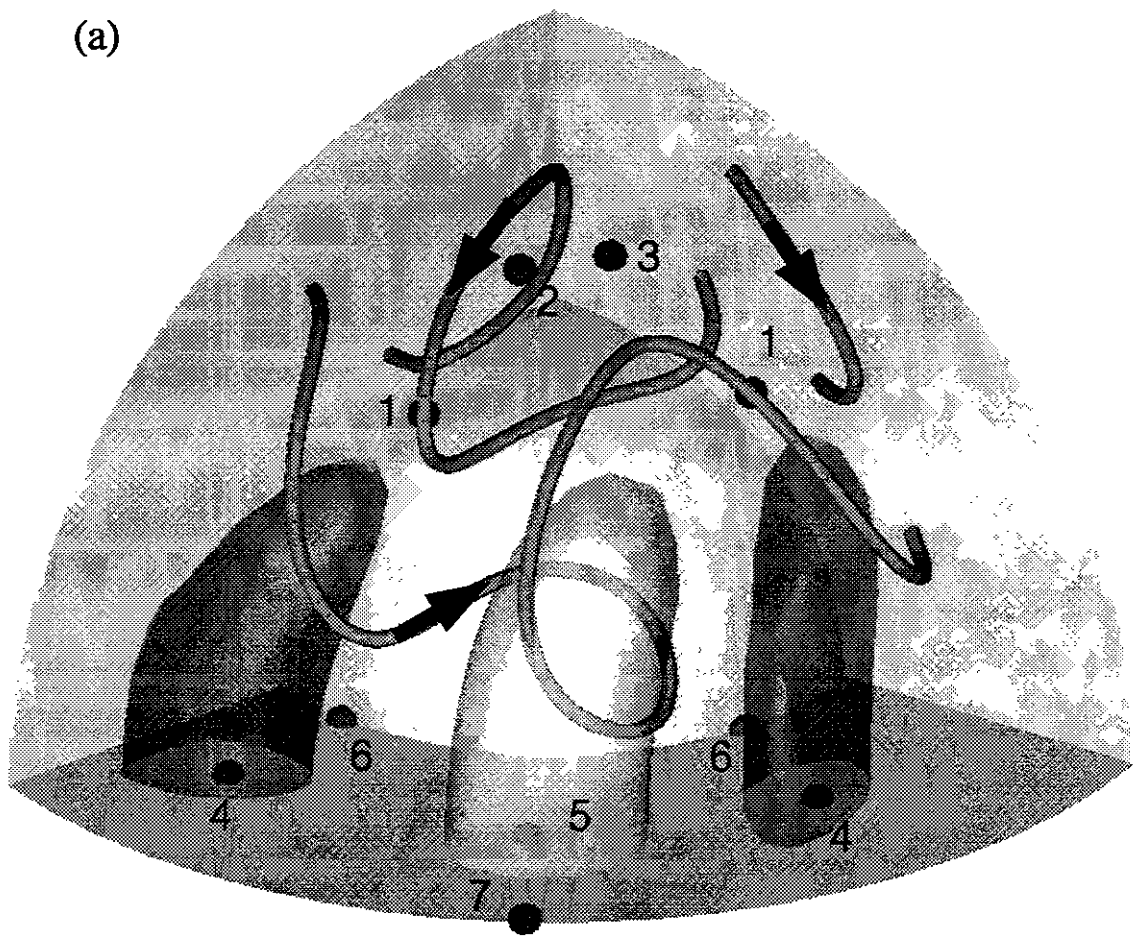

Fig.10(a)

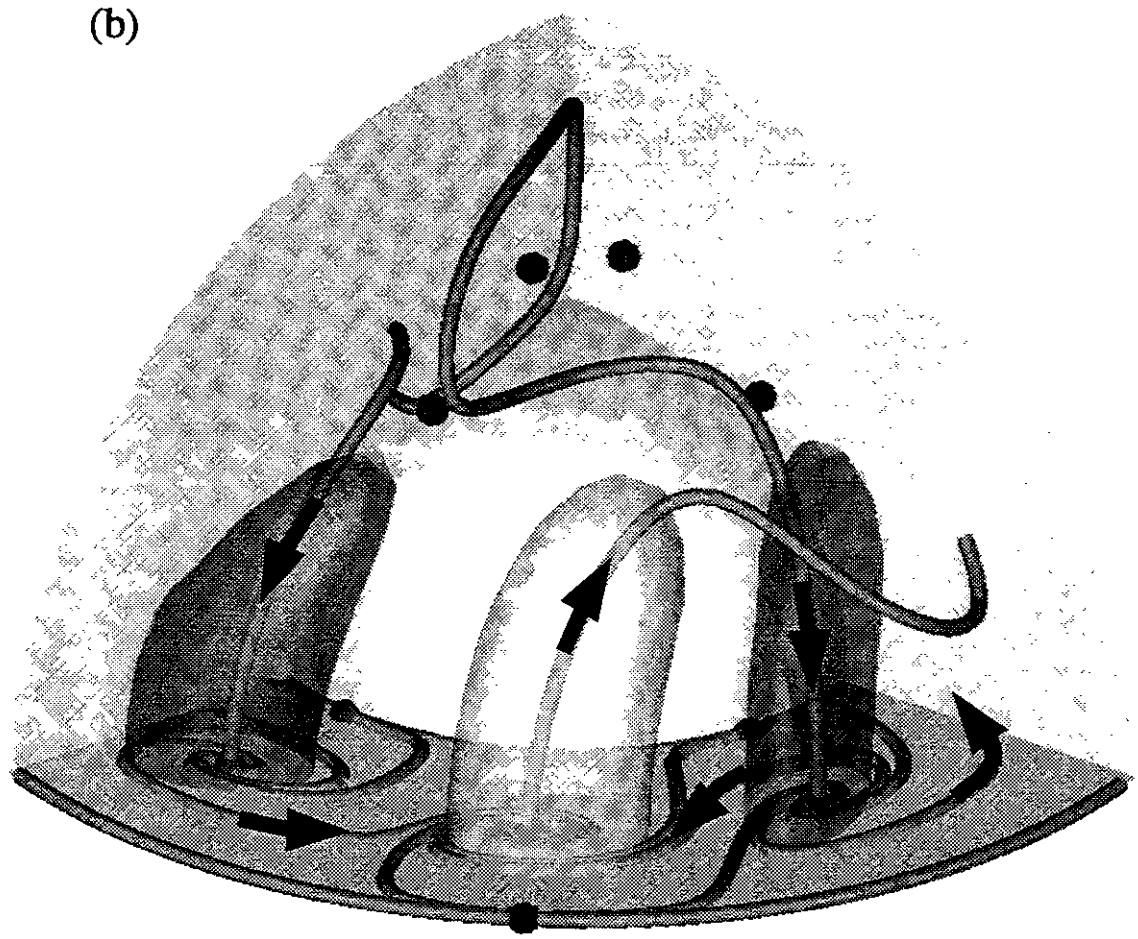

Fig.10(b)

(c)

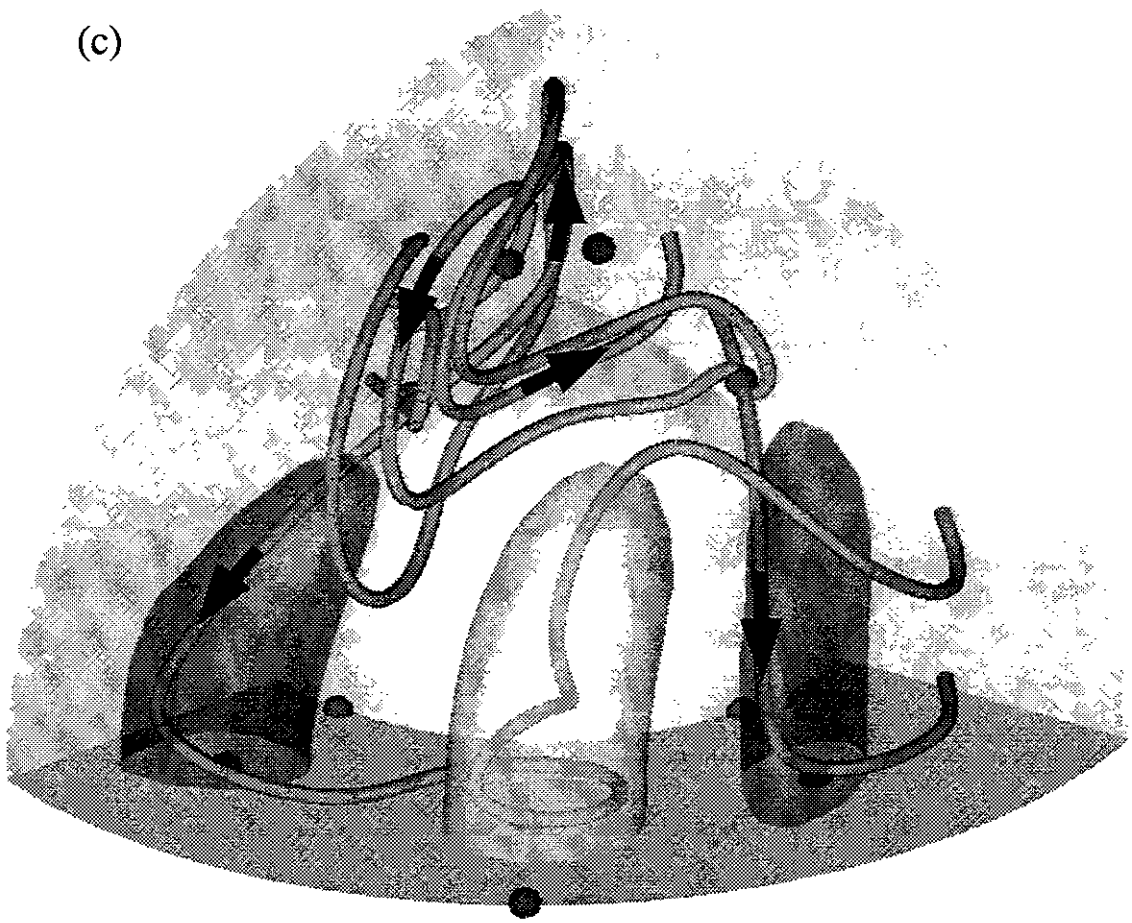

Fig.10(c)

(d)

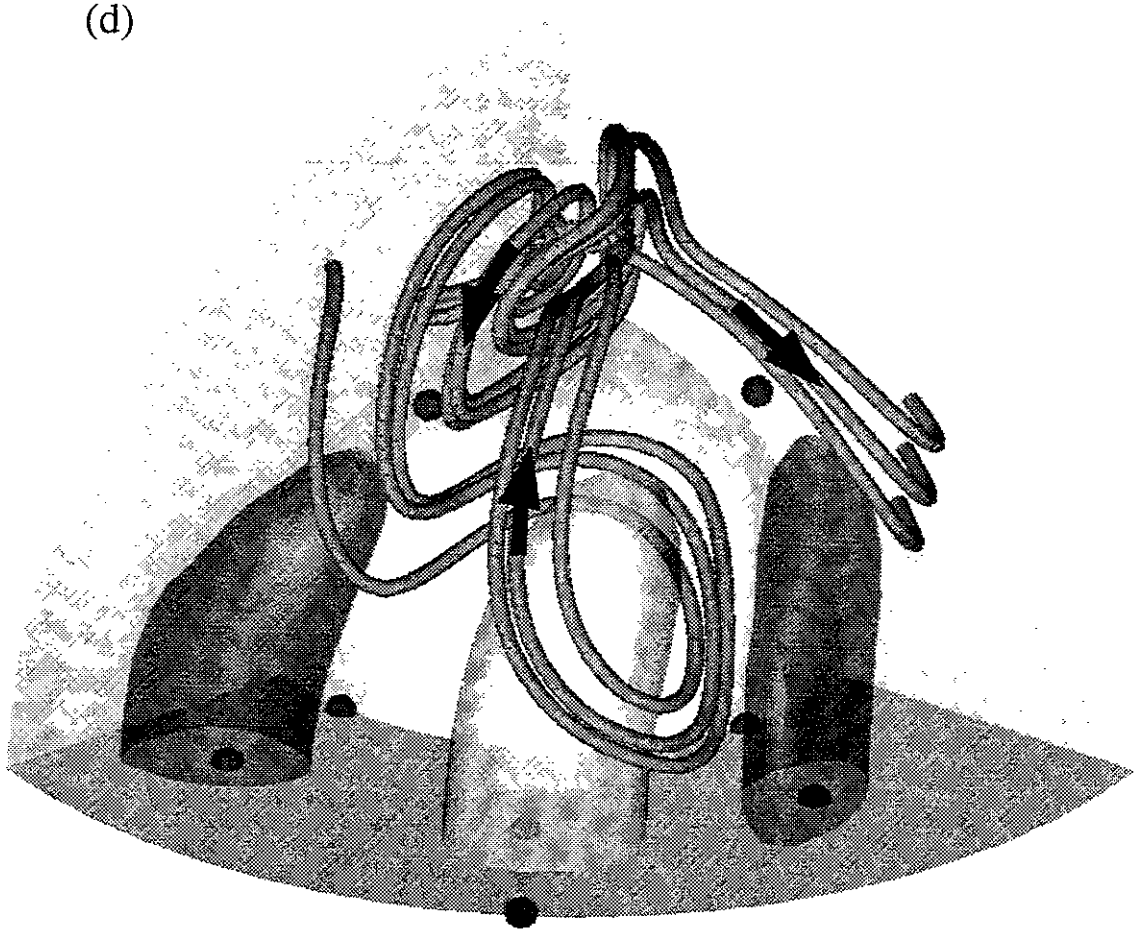

Fig.10(d)

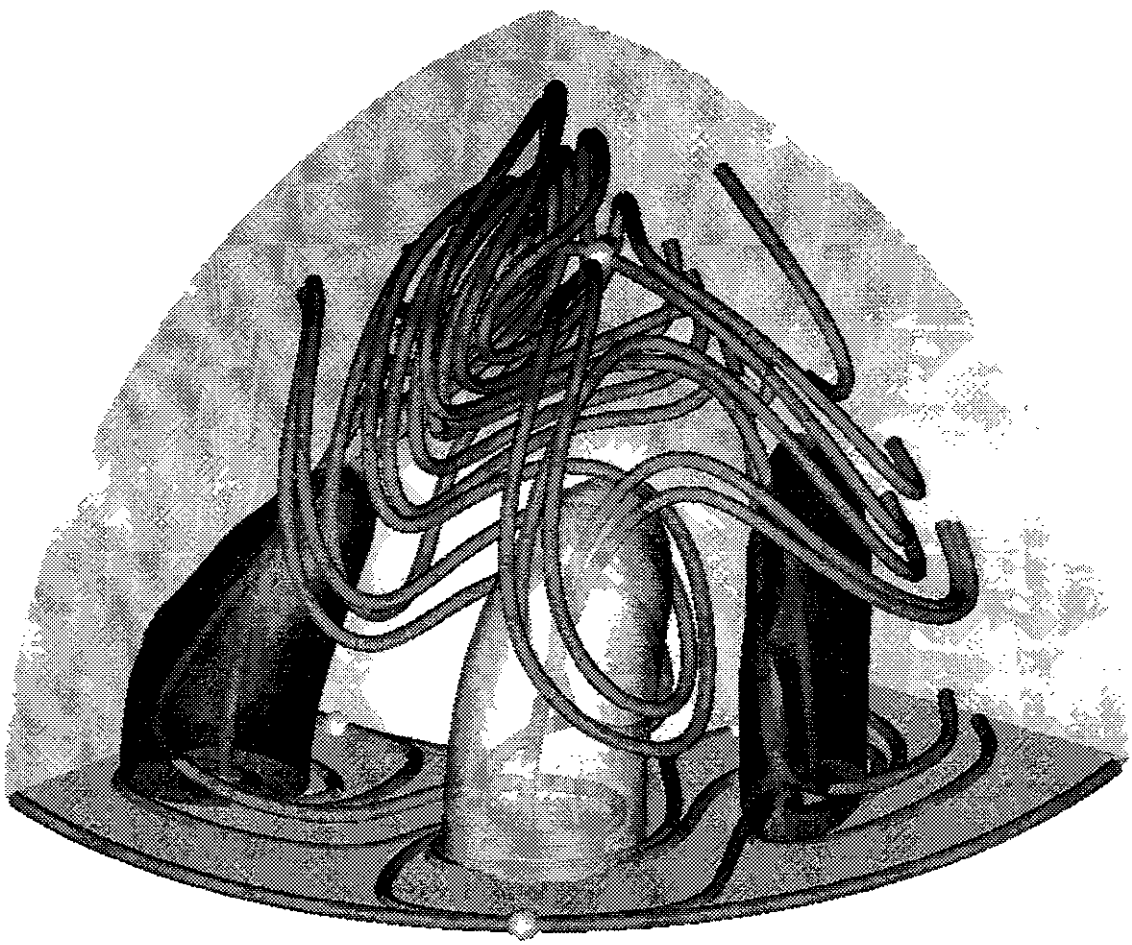

Fig.11(a)

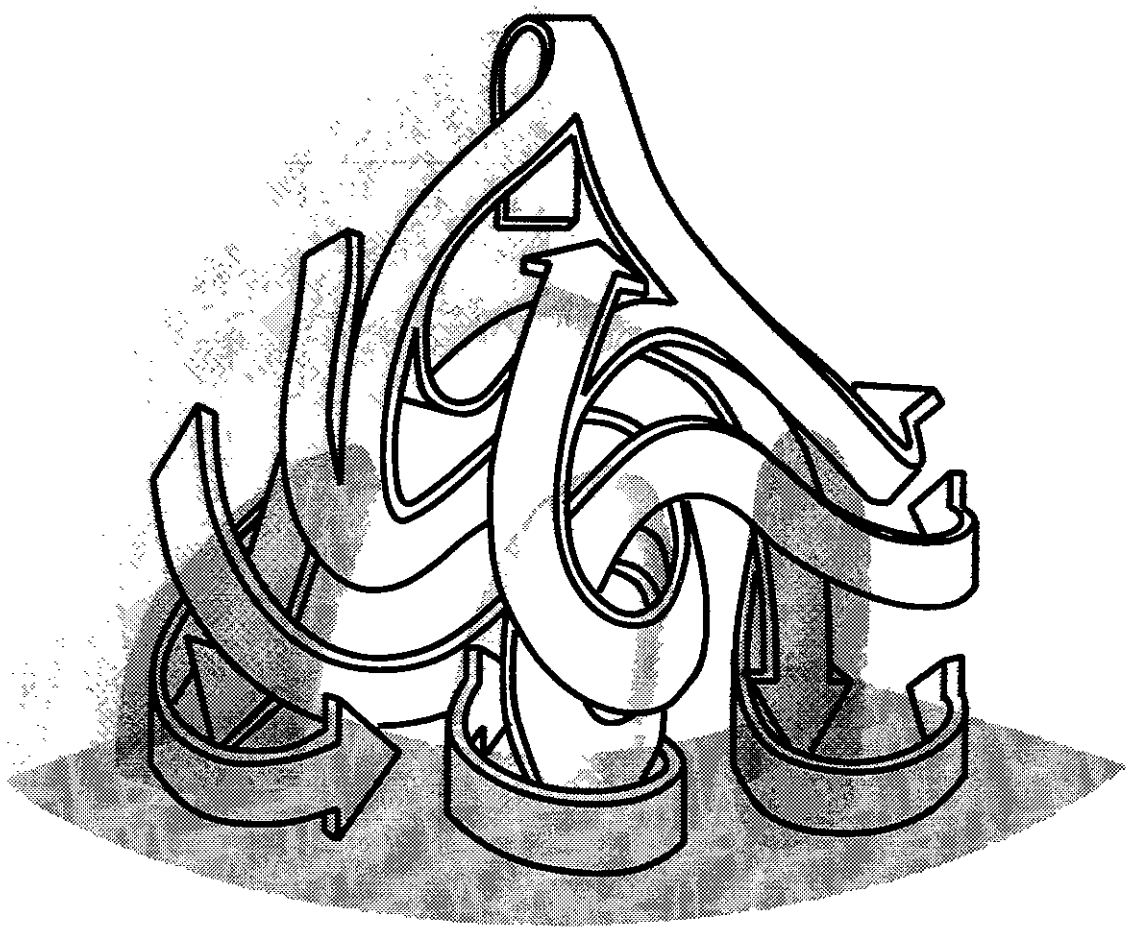

Fig.11(b)

Recent Issues of NIFS Series

NIFS-380 N. Kondo and Y. Kondoh,
Eigenfunction Spectrum Analysis for Self-organization in Dissipative Solitons, Oct. 1995

NIFS-381 Y. Kondoh, M. Yoshizawa, A. Nakano and T. Yabe,
Self-organization of Two-dimensional Incompressible Viscous Flow in a Friction-free Box; Oct. 1995

NIFS-382 Y.N. Nejoh and H. Sanuki,
The Effects of the Beam and Ion Temperatures on Ion-Acoustic Waves in an Electron Beam-Plasma System; Oct. 1995

NIFS-383 K. Ichiguchi, O. Motojima, K. Yamazaki, N. Nakajima and M. Okamoto
Flexibility of LHD Configuration with Multi-Layer Helical Coils;
Nov. 1995

NIFS-384 D. Biskamp, E. Schwarz and J.F. Drake,
Two-dimensional Electron Magnetohydrodynamic Turbulence; Nov. 1995

NIFS-385 H. Kitabata, T. Hayashi, T. Sato and Complexity Simulation Group,
Impulsive Nature in Collisional Driven Reconnection; Nov. 1995

NIFS-386 Y. Katoh, T. Muroga, A. Kohyama, R.E. Stoller, C. Namba and O. Motojima,
Rate Theory Modeling of Defect Evolution under Cascade Damage Conditions:The Influence of Vacancy-type Cascade Remnants and Application to the Defect Production Chracterization by Microstructural Analysis; Nov. 1995

NIFS-387 K. Araki, S. Yanase and J. Mizushima,
Symmetry Breaking by Differential Rotation and Saddle-node Bifurcation of the Thermal Convection in a Spherical Shell; Dec. 1995

NIFS-388 V.D. Pustovitov,
Control of Pfirsch-Schlüter Current by External Poloidal Magnetic Field in Conventional Stellarators: Dec. 1995

NIFS-389 K. Akaishi,
On the Outgassing Rate Versus Time Characteristics in the Pump-down of an Unbaked Vacuum System; Dec. 1995

NIFS-390 K.N. Sato, S. Murakami, N. Nakajima, K. Itoh,
Possibility of Simulation Experiments for Fast Particle Physics in Large Helical Device (LHD); Dec. 1995

NIFS-391 W.X.Wang, M. Okamoto, N. Nakajima, S. Murakami and N. Ohyabu,

A Monte Carlo Simulation Model for the Steady-State Plasma in the Scrape-off Layer; Dec. 1995

NIFS-392 Shao-ping Zhu, R. Horiuchi, T. Sato and The Complexity Simulation Group, *Self-organization Process of a Magnetohydrodynamic Plasma in the Presence of Thermal Conduction;* Dec. 1995

NIFS-393 M. Ozaki, T. Sato, R. Horiuchi and the Complexity Simulation Group *Electromagnetic Instability and Anomalous Resistivity in a Magnetic Neutral Sheet*; Dec. 1995

NIFS-394 K. Itoh, S.-I Itoh, M. Yagi and A. Fukuyama, *Subcritical Excitation of Plasma Turbulence*; Jan. 1996

NIFS-395 H. Sugama and M. Okamoto, W. Horton and M. Wakatani. *Transport Processes and Entropy Production in Toroidal Plasmas with Gyrokinetic Eletromagnetic Turbulence;* Jan. 1996

NIFS-396 T. Kato, T. Fujiwara and Y. Hanaoka, *X-ray Spectral Analysis of Yohkoh BCS Data on Sep. 6 1992 Flares - Blue Shift Component and Ion Abundances -;* Feb. 1996

NIFS-397 H. Kuramoto, N. Hiraki, S. Moriyama, K. Toi, K. Sato, K. Narihara, A. Ejiri, T. Seki and JIPP T-IIU Group, *Measurement of the Poloidal Magnetic Field Profile with High Time Resolution Zeeman Polarimeter in the JIPP T-IIU Tokamak*; Feb. 1996

NIFS-398 J.F. Wang, T. Amano, Y. Ogawa, N. Inoue, *Simulation of Burning Plasma Dynamics in ITER*; Feb. 1996

NIFS-399 K. Itoh, S-I. Itoh, A. Fukuyama and M. Yagi, *Theory of Self-Sustained Turbulence in Confined Plasmas*; Feb. 1996

NIFS-400 J. Uramoto, *A Detection Method of Negative Pionlike Particles from a H2 Gas Descharge Plasma*; Feb. 1996

NIFS-401 K.Ida, J.Xu, K.N.Sato, H.Sakakita and JIPP TII-U group, *Fast Charge Exchange Spectroscopy Using a Fabry-Perot Spectrometer in the JIPP TII-U Tokamak;* Feb. 1996

NIFS-402 T. Amano, *Passive Shut-Down of ITER Plasma by Be Evaporation;* Feb. 1996

NIFS-403 K. Orito, A New Variable Transformation Technique for the Nonlinear Drift Vortex; Feb. 1996

NIFS-404 T. Oike, K. Kitachi, S. Ohdachi, K. Toi, S. Sakakibara, S. Morita, T. Morisaki,

H. Suzuki, S. Okamura, K. Matsuoka and CHS group; *Measurement of Magnetic Field Fluctuations near Plasma Edge with Movable Magnetic Probe Array in the CHS Heliotron/Torsatron*; Mar. 1996

NIFS-405 S.K. Guharay, K. Tsumori, M. Hamabe, Y. Takeiri, O. Kaneko, T. Kuroda, *Simple Emittance Measurement of H- Beams from a Large Plasma Source*; Mar. 1996

NIFS-406 M. Tanaka and D. Biskamp, *Symmetry-Breaking due to Parallel Electron Motion and Resultant Scaling in Collisionless Magnetic Reconnection*; Mar. 1996

NIFS-407 K. Kitachi, T. Oike, S. Ohdachi, K. Toi, R. Akiyama, A. Ejiri, Y. Hamada, H.Kuramoto, K. Narihara, T. Seki and JIPP T-IIU Group, *Measurement of Magnetic Field Fluctuations within Last Closed Flux Surface with Movable Magnetic Probe Array in the JIPP T-IIU Tokamak*; Mar. 1996

NIFS-408 K. Hirose, S. Saito and Yoshi.H. Ichikawa *Structure of Period-2 Step-1 Accelerator Island in Area Preserving Maps*; Mar. 1996

NIFS-409 G.Y.Yu, M. Okamoto, H. Sanuki, T. Amano, *Effect of Plasma Inertia on Vertical Displacement Instability in Tokamaks*; Mar. 1996

NIFS-410 T. Yamagishi, *Solution of Initial Value Problem of Gyro-Kinetic Equation*; Mar. 1996

NIFS-411 K. Ida and N. Nakajima, *Comparison of Parallel Viscosity with Neoclassical Theory*; Apr. 1996

NIFS-412 T. Ohkawa and H. Ohkawa, *Cuspher, A Combined Confinement System*; Apr. 1996

NIFS-413 Y. Nomura, Y.H. Ichikawa and A.T. Filippov, *Stochasticity in the Josephson Map*; Apr. 1996

NIFS-414 J. Uramoto, *Production Mechanism of Negative Pionlike Particles in H_2 Gas Discharge Plasma*; Apr. 1996

NIFS-415 A. Fujisawa, H. Iguchi, S. Lee, T.P. Crowley, Y. Hamada, S. Hidekuma, M. Kojima, *Active Trajectory Control for a Heavy Ion Beam Probe on the Compact Helical System*; May 1996

NIFS-416 M. Iwase, K. Ohkubo, S. Kubo and H. Idei *Band Rejection Filter for Measurement of Electron Cyclotron Emission*

during Electron Cyclotron Heating; May 1996

NIFS-417 T. Yabe, H. Daido,T. Aoki, E. Matsunaga and K. Arisawa,
Anomalous Crater Formation in Pulsed-Laser-Illuminated Aluminum Slab and Debris Distribution; May 1996

NIFS-418 J. Uramoto,
Extraction of K^- Mesonlike Particles from a D_2 Gas Discharge Plasma in Magnetic Field; May 1996

NIFS-419 J. Xu, K. Toi, H. Kuramoto, A. Nishizawa, J. Fujita, A. Ejiri, K. Narihara, T. Seki, H. Sakakita, K. Kawahata, K. Ida, K. Adachi, R. Akiyama, Y. Hamada, S. Hirokura, Y. Kawasumi, M. Kojima, I. Nomura, S. Ohdachi, K.N. Sato
Measurement of Internal Magnetic Field with Motional Stark Polarimetry in Current Ramp-Up Experiments of JIPP T-IIU; June 1996

NIFS-420 Y.N. Nejoh,
Arbitrary Amplitude Ion-acoustic Waves in a Relativistic Electron-beam Plasma System; July 1996

NIFS-421 K. Kondo, K. Ida, C. Christou, V.Yu.Sergeev, K.V.Khlopenkov, S.Sudo, F. Sano, H. Zushi, T. Mizuuchi, S. Besshou, H. Okada, K. Nagasaki, K. Sakamoto, Y. Kurimoto, H. Funaba, T. Hamada, T. Kinoshita, S. Kado, Y. Kanda, T. Okamoto, M. Wakatani and T. Obiki,
Behavior of Pellet Injected Li Ions into Heliotron E Plasmas; July 1996

NIFS-422 Y. Kondoh, M. Yamaguchi and K. Yokozuka,
Simulations of Toroidal Current Drive without External Magnetic Helicity Injection; July 1996

NIFS-423 Joong-San Koog,
Development of an Imaging VUV Monochromator in Normal Incidence Region; July 1996

NIFS-424 K. Orito,
A New Technique Based on the Transformation of Variables for Nonlinear Drift and Rossby Vortices; July 1996

NIFS-425 A. Fujisawa, H. Iguchi, S. Lee, T.P. Crowley, Y. Hamada, H. Sanuki, K. Itoh, S. Kubo, H. Idei, T. Minami, K. Tanaka, K. Ida, S. Nishimura, S. Hidekuma, M. Kojima, C. Takahashi, S. Okamura and K. Matsuoka,
Direct Observation of Potential Profiles with a 200keV Heavy Ion Beam Probe and Evaluation of Loss Cone Structure in Toroidal Helical Plasmas on the Compact Helical System; July 1996

NIFS-426 H. Kitauchi, K. Araki and S. Kida,
Flow Structure of Thermal Convection in a Rotating Spherical Shell; July 1996